Journal of Materials Chemistry A

ROYAL SOCIETY OF CHEMISTRY

REVIEW

View Article Online
View Journal

Cite this: DOI: 10.1039/d6ta02123a

Oxy-sulfide semiconductors for hydrogen production from pure water: materials design, performance, and stability

Olzat Toktarbaiuly,*[a] Mergen Zhazitov,[a] Nazerke Kydyrbay,[a] Tolagay Duisebayev,[a] Yerbolat Tezekbay,[a] Nurxat Nuraje,[ab] Muhammad Abdullah*[a] and Hicham Idriss*[c]

Received 11th March 2026
Accepted 4th May 2026

DOI: 10.1039/d6ta02123a

rsc.li/materials-a

Oxy-sulfides have emerged as a versatile class of mixed-anion semiconductors capable of bridging the complementary strengths of oxides (structural stability) and sulfides (narrow band gap, enhanced conductivity) for hydrogen production from pure water. This review summarises recent progress in their application as both photocatalysts and electrocatalysts, with emphasis on mixed-anion electronic structure, band-edge engineering, and charge-carrier dynamics. Layered titanate oxy-sulfides, exemplified by $Y_2Ti_2O_5S_2$, are highlighted as benchmarks for visible-light-driven overall water splitting; key findings regarding cocatalyst loading effects, band-tail states, and interfacial selectivity are critically assessed. Electrocatalytic systems—notably NiFe-based oxy-sulfides—are also reviewed, with attention to the role of sulfur content, *in situ* reconstruction, and active-phase evolution. Degradation mechanisms including photocorrosion, surface reconstruction, and compositional drift are discussed alongside mitigation strategies. Despite substantial progress, solar-to-hydrogen efficiencies in pure-water systems remain well below levels required for practical deployment. Future directions involving *operando* characterisation, first-principles-guided materials design, and scalable synthesis are outlined.

1. Introduction

Hydrogen is central to visions of a low-carbon energy system, both as a clean fuel and as a key feedstock for major industrial processes. Unlike energy carriers derived from fossil fuels, hydrogen can be produced *via* pathways with no direct greenhouse-gas emissions, making it an anchor for climate-neutral energy strategies. Many projections suggest that hydrogen could supply ~20–25% of global energy demand by mid-century as production shifts toward renewable routes.[1] Renewable hydrogen can be generated through several pathways; the three most common – thermochemical, photochemical, and electrochemical – are summarized in Fig. 1.[2,3]

Despite these promises, current hydrogen production remains dominated by steam methane reforming and coal gasification, which together account for more than 95% of global supply and are responsible for substantial CO_2 emissions.[4] This reliance on carbon-intensive processes motivates the development of scalable and sustainable alternatives. In this context, water splitting driven either by renewable electricity (electrocatalysis) or directly by sunlight (photocatalysis) is an especially attractive route to "green hydrogen".[5,6]

The performance and practicality of water splitting are governed by the availability of catalysts and semiconductors that are simultaneously active, durable, and possibly composed of earth-abundant elements. To date, the highest-performing catalysts for the hydrogen evolution reaction (HER) and oxygen evolution reaction (OER) often rely on noble metals such as Pt, Ir, and Ru. Their scarcity and high cost, however, severely limit large-scale deployment.[7] This has driven intense research into alternative material classes, including transition-metal oxides, sulfides, phosphides, and carbides.[8,9] Each class, however, has intrinsic limitations: oxides are generally robust but frequently suffer from wide band gap energies (limited visible-light absorption), whereas sulfides exhibit favorable optical and electronic properties but are often unstable under photo- or electrochemical operating conditions.

In photocatalysis in particular, it is important to distinguish between overall water splitting in pure water and half-reaction systems driven by sacrificial agents. A large fraction of the literature reports hydrogen evolution in the presence of sacrificial electron donors (*e.g.*, alcohols, sulfide/sulfite mixtures, or amines), and/or electron acceptors (*e.g.*, Ag^+, IO_3^-) which suppress recombination and photocorrosion but do not

[a]Renewable Energy Laboratory, National Laboratory Astana (NLA), Nazarbayev University, Kabanbay Batyr 53, Astana 010000, Kazakhstan. E-mail: olzat.toktarbaiuly@nu.edu.kz; muhammad.abdullah@nu.edu.kz

[b]Department of Chemical and Materials Engineering, School of Engineering and Digital Sciences, Nazarbayev University, Astana 010000, Kazakhstan

[c]Department of Chemistry, University College London, London WC1E 6BT, UK. E-mail: h.idriss@ucl.ac.uk

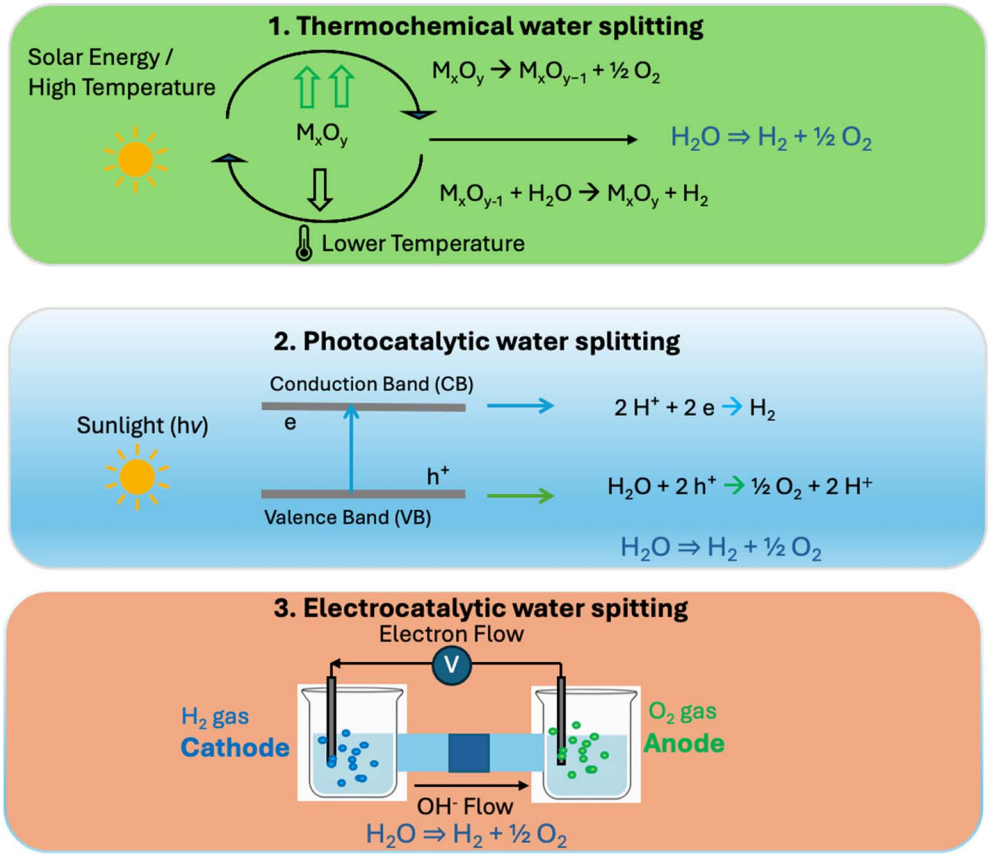

Fig. 1 Basic principles presenting the thermochemical, photochemical and electrochemical reactions for hydrogen production from water.

represent true water splitting. While such systems are valuable for mechanistic insight, they are inherently misleading when assessing practical viability: sacrificial agents increase cost, complicate system design, generate[10] CO_2, may precipitate[11–13] and poison the catalytic sites, and often stabilize materials that would otherwise degrade under overall water-splitting conditions. Consequently, performance metrics reported under sacrificial conditions cannot be translated to realistic solar hydrogen production. This distinction between sacrificial-agent-driven hydrogen evolution and true overall water splitting is essential, as only the latter reflects the thermodynamic, kinetic, and stability constraints relevant to catalytic water splitting materials.

From a techno-economic perspective, overall water splitting in pure water remains the relevant benchmark. In this context, the solar-to-hydrogen (STH) efficiency is a critical metric, and values of at least ~10% are generally regarded as a lower bound for economic feasibility.[14] Most photocatalytic systems reported to date—including oxysulfide-based materials—still operate at STH efficiencies well below 1% under pure-water conditions, underscoring the substantial gap between laboratory demonstrations and practical requirements.

Before discussing specific oxy-sulfide systems, it is instructive to contrast the key properties of oxide, sulfide, and oxy-sulfide semiconductors. Oxide semiconductors (*e.g.*, TiO_2, $SrTiO_3$) typically exhibit wide band gaps (above 3.0 eV), restricting light absorption to the UV region (less than 5% of the solar photon flux), but possess excellent structural and chemical stability under aqueous conditions owing to the high lattice energy of M–O bonds. Sulfide semiconductors (*e.g.*, CdS, In_2S_3) benefit from narrower band gaps (1.8–2.4 eV) compatible with visible-light harvesting and higher electronic conductivity from the more polarisable S^{2-} anion, but suffer from photocorrosion and dissolution in pure water under prolonged illumination. Oxy-sulfide semiconductors combine aspects of both: the mixed-anion lattice narrows the band gap relative to the parent oxide through upward VBM shifting driven by S 3p states, while partial retention of M–O bonds preserves structural robustness relative to the pure sulfide. The O/S ratio and local coordination geometry provide independent design parameters for simultaneously tuning band gap, band edge positions, carrier mobility, and long-term stability, a degree of compositional flexibility unavailable in single-anion materials.[15–17]

Oxy-sulfides have re-emerged as a promising hybrid class in this regard. By combining oxide-like structural stability with sulfide-like electronic and optical properties, mixed-anion oxy-sulfides offer a design space in which band edges, defect states, and charge-carrier dynamics can be tuned through anion composition, local ordering, and symmetry breaking.[18,19] Recent progress including layered perovskite-type oxysulfide photocatalysts capable of visible-light-driven overall water splitting and oxy-sulfide electrocatalysts derived from controlled

sulfidation/oxidation pathways has created a timely opportunity to critically assess both their potential and their limitations.

Several existing reviews focus broadly on metal sulfide photocatalysts or oxide-based systems, often emphasizing half-reaction photocatalysis in the presence of sacrificial agents. By contrast, this review deliberately focuses on oxy-sulfide materials evaluated under pure-water conditions, with particular attention to: (i) mixed-anion electronic structure and band energy engineering, (ii) structure–property relationships, (iii) photocatalytic and electrocatalytic hydrogen production metrics relevant to overall water splitting, and (iv) deactivation mechanisms and scalability constraints. Through this, we aim to clarify both the promise of oxy-sulfides and the challenges that must be overcome to approach technologically meaningful STH efficiencies.

2. Fundamental principles and the electronic structure of oxy-sulfides

2.1. Introduction to water splitting

Hydrogen can be produced (non-thermally) from water splitting through two primary mechanisms: electrocatalysis and photocatalysis. HER is an electrochemical process that occurs through multiple steps, including adsorption, reduction, and desorption on/from the electrode surface, culminating in the formation of H_2.[7] The reaction may proceed according to the following steps:[7]

$$H_2O + e^- \rightleftarrows H_{ads} + OH^- \text{ (Volmer step)} \quad (1)$$

$$H_{ads} + H_2O + e^- \rightleftarrows H_2 + OH^- \text{ (Heyrovsky step)} \quad (2)$$

$$2H_{ads} \rightleftarrows H_2 \text{ (Tafel step)} \quad (3)$$

The HER starts with the Volmer step, where a water molecule is dissociated (to H^+ and OH^-) followed by proton adsorption onto the electrode then upon electron transfer gives an adsorbed hydrogen atom. Further reactions occur, either through the Heyrovsky step, where the adsorbed hydrogen atom reacts with the electrolyte proton and another electron to give H_2, or the Tafel step, where two adsorbed hydrogen atoms combine to release H_2. Most studies have indicated that at high potentials the Tafel step is less significant, and the Volmer–Heyrovsky route dictates the HER mechanism.

Photocatalytic water splitting (PCWS) utilizes light to transfer electrons from the valence band (VB) to the conduction band (CB) of a semiconductor, and the resulting electrons and holes induce hydrogen evolution and water oxidation, respectively. To achieve spontaneous overall splitting, the CB edge must be more negative than the H^+/H_2 potential and the VB edge more positive than the H_2O/O_2 potential. These are equivalent to about −0.41 V and +0.82 V with respect to the normal hydrogen electrode (NHE) at pH 7. While the theoretical requirement of 1.23 eV per electron is needed to split water to H_2 and O_2, in practice because of the many losses associated to each reaction step (grouped together by the "so-called" overpotential) semiconductors with band gap above 1.8 eV are needed.

2.2. Introduction to oxysulfides

Oxy-sulfides are of particular interest because the presence of sulfur (i) decreases the band gap energy, (ii) raises the CB and (iii) keeps the VB oxidation potential low enough to allow for hole transfer.

Before presenting and discussing some of them and their associated activity, it is worth indicating a few points related to the differences between oxides, sulfides and oxy-sulfides band gap energies.

2.2.1 Electronegativity of the anion strongly influences the energy of the valence band (VB) of a semiconductor. Highly electronegative anions (*e.g.*, O^{2-}) hold their electrons tightly and therefore their p orbitals lie at low (more negative) energy. This results in a deep VB energy which in turn gives a large band gap energy (E_g).[20,21] Less electronegative anions (*e.g.*, S^{2-}) hold electrons less tightly and therefore their p orbitals lie at higher (less negative) energy. This results in a shallower VB energy which in turn gives a small E_g. The CB is mostly dominated by metal cation d (or in some cases p) orbitals, so the primary E_g change comes from the upward shift of the VB.

2.2.2 Orbital energies, size and overlap. Because of (a) oxygen 2p orbitals are lower in energy than sulfur 3p orbitals. When these anion orbitals hybridize with metal cation orbitals and since the CB (dominated by metal d orbitals) does not shift much, E_g shrinks when S replaces O.

2.2.3 Mixed-anion oxysulfides have therefore tunable band gaps as presented in Table 1. Thus, lower electronegativity associated to higher p-orbital energy gives higher VB which results in smaller band gap energies.

The superior band structure flexibility of mixed-anion oxysulfides relative to single-anion semiconductors arises from the co-existence of O^{2-} and S^{2-} in the same lattice. In single-anion semiconductors (pure oxides or pure sulfides), the valence band derives from a single anion p-orbital type whose energy is fixed by the element's electronegativity, leaving little scope for tuning without entirely replacing the metal cation. In oxysulfides, by contrast, both O 2p and S 3p states contribute to the valence band through indirect hybridisation mediated by the bridging metal cation (O 2p ↔ M^{n+} d ↔ S 3p). Because O^{2-} and S^{2-} differ markedly in electronegativity (3.44 *vs.* 2.58 on the Pauling scale), polarizability (~3.0 *vs.* ~7.0 Å^3), and ionic radius (1.40 *vs.* 1.84 Å), continuously varying the O/S ratio tunes the energy of the hybrid valence band without significantly perturbing the conduction band (dominated by metal d/p states). This provides a two-dimensional handle on the band gap: the S fraction controls VBM elevation while the cation identity controls CBM position—a degree of flexibility unachievable in single-anion materials. Furthermore, the ionic size mismatch between O^{2-} and S^{2-} introduces local lattice strain and polar distortions that can shift band edges by 0.4–0.7 eV and generate built-in electric fields, discussed further in Section 2.4.

2.2.4 O and S anions orbitals mix due to indirect hybridization through metal cations. In metal oxysulfides (*e.g.*, O–M–S–M′ systems) O^{2-} is bonded to the metal (M^{x+}), S^{2-} is also bonded to M^{x+} or M'^{y+}. The M (M′) cation has empty or partially filled d orbitals (or p orbitals depending on the metal). Thus,

Table 1 Comparison between oxide and sulfide semiconductors band gap energies

Anion	Electronegativity	P-orbital energy	VB position	Band gap, E_g
O^{2-}	High	Low	Deep	Large E_g
S^{2-}	Lower	Higher	Raised	Smaller E_g

Table 2 Photocatalytic activity of $Y_2Ti_2O_5S_2$ for overall water splitting. Calcination temperatures and pH effects on reaction rates of H_2 and O_2 production from water on Cr_2O_3/Rh/IrO_2-modified $Y_2Ti_2O_5S_2$ in distilled water buffered by La_2O_3. For the pH effect the $Y_2Ti_2O_5S_2$ was calcined at 1073 K. Reactions were carried out under illumination from a xenon lamp (300 W, $\lambda > 420$ nm). Extracted numbers from ref. 22, are within ±10%

Calcination temperature			pH			
	973 K	1073 K	6.8	8	9	10
H_2 (μmol h^{-1})	7.5	2	0.1	2.3	2.5	0.1
O_2 (μmol h^{-1})	4	1	—	1.2	1.2	—

both O 2p and S 3p orbitals overlap with the metal d (or p) orbitals, and therefore become part of the same extended band. This leads to indirect hybridization pathway:

$$O^{2-}\ 2p \leftarrow\rightarrow M^{x+}\ nd \leftarrow\rightarrow S^{2-}\ 3p \quad (4)$$

Because both O^{2-} and S^{2-} interact with the metal's electronic states, the resulting band is a linear combination of all three sets of orbitals. Also, because S 3p and metal d orbitals are much closer in energy, S mixes strongly with the metal, pulling the valence band upward. In short, because the band is delocalized across the whole crystal, the O 2p states also admix without direct O–S bonding.

2.3. Examples of oxy-sulfides active as photocatalysts for pure water splitting

One of the first successful examples for overall water system based on oxy-sulfides[22] is $Y_2Ti_2O_5S_2$. In order to make it a photocatalyst, it was further modified by IrO_2 (for O_2 production) and Rh (for H_2 production). In addition, Rh particles were protected by Cr_2O_3, largely to prevent H_2/O_2 re-combination back to water. It has a band gap energy of 1.9 eV and splits

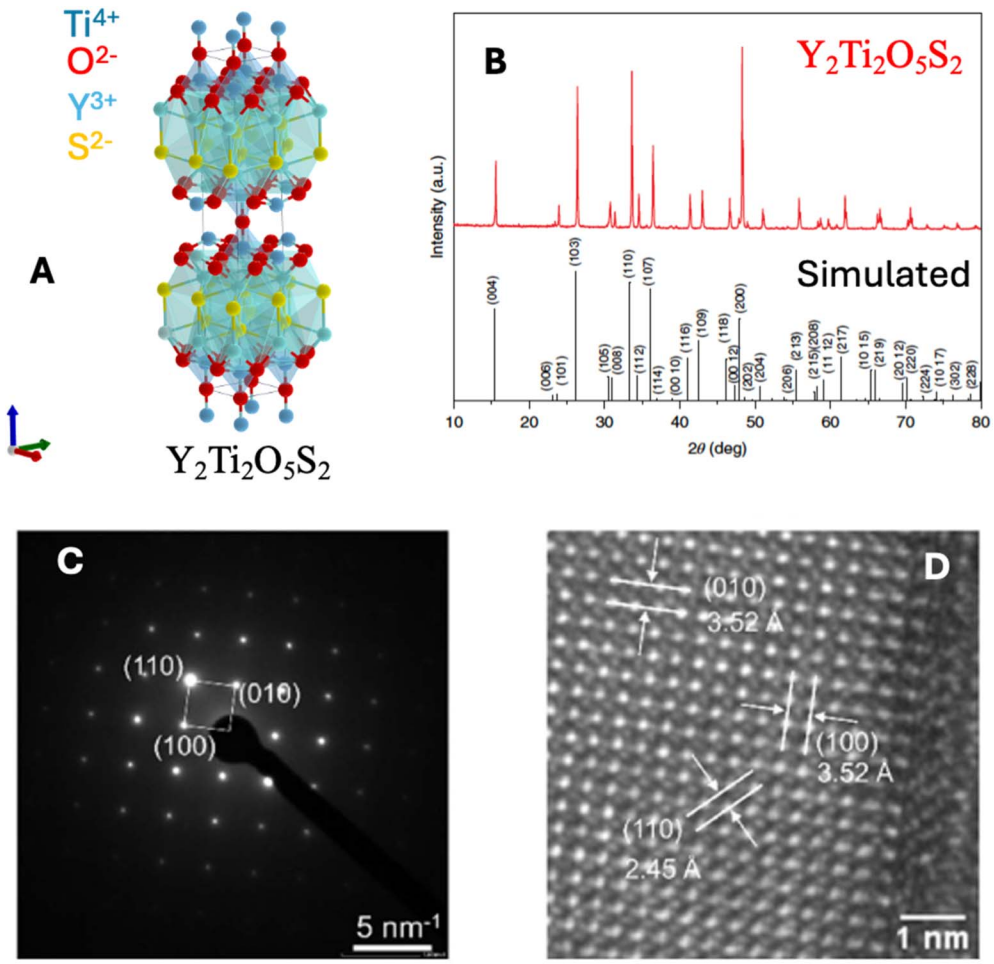

Fig. 2 Structure of $Y_2Ti_2O_5S_2$. (A) The crystal structure from Materials Project,[26] (B) its analyzed XRD pattern (red spectra) and simulated data (black spectra). (C) SAED pattern, (D) HRTEM image (f). From ref. 28.

water in a narrow pH window (8–9), Table 2. Annealing at 973 K was found best and with an STH efficiency, eqn (5), of 0.007% (the theoretical maximum STH efficiency at this band gap energy is 20.9%) and was stable for a 20 h test duration.

$$\mathrm{STH}(\%) = \frac{(R(\mathrm{H_2}) \times \Delta G_r)}{(P \times S)} \times 100 \quad (5)$$

$R(H_2)$, ΔG_r, P and S are for the rate of H_2 production, the Gibbs free energy of the water-splitting reaction, light flux of the AM 1.5 G solar irradiation (100 mW cm^{-2}) and the irradiated sample area, respectively.

Fig. 2 presents the structure and corresponding XRD patterns of this oxysulfide semiconductor. The $Y_2Ti_2O_5S_2$ unit cell comprises alternating rocksalt slabs $[Y_2S_2]^{2+}$ and ReO_3-type blocks formed from –(TiO_2)–(O)–(TiO_2)-layers stacked along the *c*-direction. Fig. 3 and 4 show the dependency of the ratio O_2 to H_2 ratio as well as production on the loading amounts of Cr, Ir and Rh. It is important to mention that the default catalyst contains 0.3, 2 and 1.5 wt% of Ir, Rh and Cr and it is understood that two are fixed while changing the % of the third component while testing their effect. As is often the case for photocatalytic materials, the activity saturates very fast with the amount of metal loaded and sometimes decreases after a narrow threshold (typically between 0.5 and 2 wt%).[23–25]

In the case of the IrO_2 series, the ratio starts very low (~0.18), then gradually increases up to 0.5 at high loading. This means that at low loading O_2 evolution is strongly suppressed relative to H_2 and this is due to either slow OER kinetics or strong back reaction. As the amount of IrO_2 increases OER kinetics improve and O_2 catches up toward stoichiometric value and this is consistent with IrO_2 acting primarily as an OER cocatalyst.

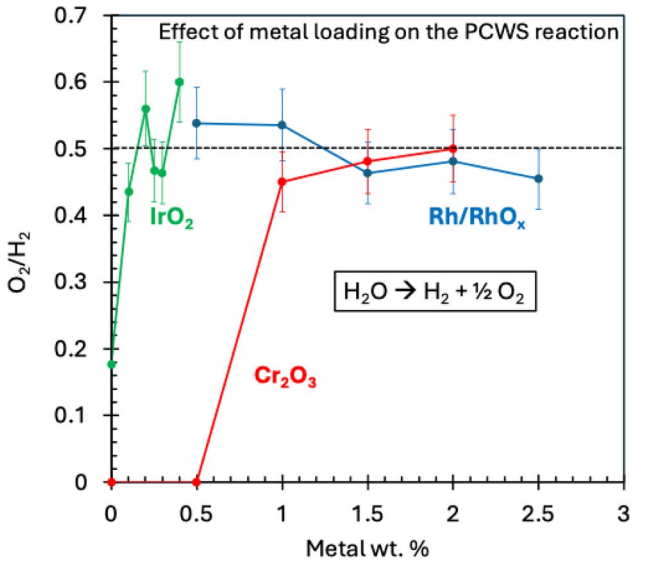

Fig. 3 Effect of amount of Ir, Rh and Cr in wt% on the O_2/H_2 ratio during the reaction of $Y_2Ti_2O_5S_2$ for overall photo-catalytic water splitting (PCWS). The reactions were carried out under 300 W Xe lamp illumination (λ > 420 nm) in distilled water buffered by La_2O_3 (pH 8.5). Data computed from ref. 22.

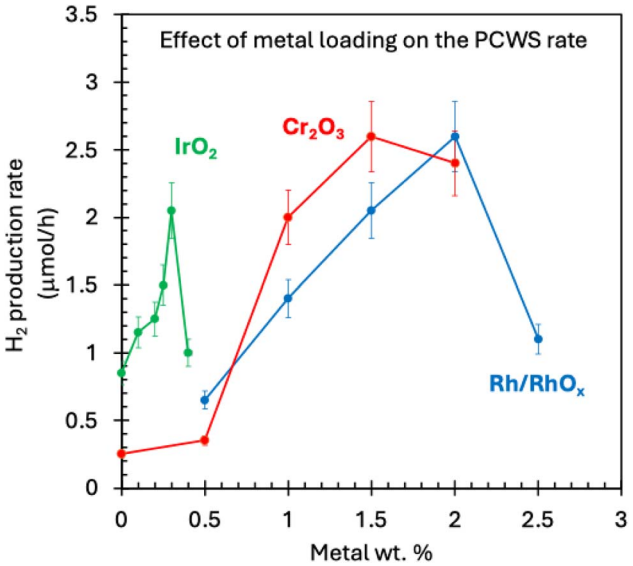

Fig. 4 Effect of amount of Ir, Rh and Cr in wt% on the H_2 production rate during the reaction of $Y_2Ti_2O_5S_2$ for overall photo-catalytic water splitting (PCWS). The reactions were carried out under 300 W Xe lamp illumination (λ > 420 nm) in distilled water buffered by La_2O_3 (pH 8.5). Data computed from ref. 22.

For the Rh series, the ratio is already near ~0.5 even at low loading. While this indicates that the system is more balanced, the absolute rates are still lower at low loading. At high Rh loading, there is a slight drop in the ratio which may suggest a slight recombination enhancement. For the Cr series, probably the most interesting, at 0–0.5 wt% the ratio ≈0 (essentially no measurable O_2), then at 1.0 wt% there is a sudden jump to ~0.45, followed by a stabilization near 0.5. This is not gradual there is a threshold-like behavior. This strongly suggests that at low Cr_2O_3, O_2 is being generated but consumed (back reaction). Once Cr reaches ~1 wt%, a protective/selective layer forms on Rh, back reaction is suppressed as well as, possibly, that of O_2 reduction reaction (ORR) on Rh. These data suggest that the dominant limitation at low cocatalyst loading is surface recombination/back reaction, not bulk charge recombination. Also, Cr_2O_3 is acting as a reaction-selectivity modulator, not a cocatalyst. Once surface selectivity is fixed, the system approaches stoichiometric splitting, but absolute rates are still modest. This may indicate that efficiency is, in addition to bandgap engineering, mostly about surface reaction selectivity and suppression of non-desired pathways. In other words, performance is not limited by absorption or band alignment, but by interfacial charge-selectivity and recombination suppression (Fig. 2).

It is instructive to compare such data with those expected if an electron scavenger such as Ag ions is used where in such a case there is no H_2 evolution but O_2 is made. At low Cr loading, $O_2/H_2 \approx 0$, yet H_2 is produced. That means, either O_2 is being reduced back (back reaction), or holes are not efficiently transferred to OER sites, and/or surface recombination dominates. Once Cr reaches ~1–1.5 wt% (knowing that Rh is fixed at 2 wt%) O_2/H_2 tends to 0.5 and the system approaches true

overall splitting stoichiometry. In a typical $AgNO_3$ system, electrons are scavenged immediately. O_2 reduction cannot occur and back reaction is artificially suppressed. The system appears stable and active. In other words, sacrificial systems artificially enforce the equivalent of a "perfect Cr_2O_3 layer." Those point out that the dominant loss channel is surface recombination and back reaction, not bulk bandgap limitation. This explains why many systems show good half-reaction performance, but very low STH in pure water, if at all. This is because the bottleneck is not photon absorption alone—it is charge-selectivity at interfaces.

Fig. 4 shows the expected "optimum loading" behavior for each series (IrO_2, Rh, Cr_2O_3). The Rh and Cr series show strong increases up to ~2 wt% (Rh) and ~1.5 wt% (Cr_2O_3), then a drop/plateau. This is consistent with what has been seen for decades for half reaction (photo-reforming of alcohols, for example). The IrO_2 series peaks sharply around 0.3 wt%, then drops at 0.4 wt%, which may indicate a more complex and certainly less known interfacial effects.

Focusing on the profile of H_2 as a function of Cr_2O_3 and Rh loading, the curves look remarkably similar, both show a strong rise, both peak near ~1.5–2 wt%, and both decline at higher loading. At first glance that looks redundant but it actually reveals something important. Even though one is nominally fixed while the other varies, the system is interfacially coupled. Rh and Cr_2O_3 are not acting separately. Rh is the HER metal, Cr forms a thin Cr_2O_3 overlayer on Rh. So, when the amounts of Rh changes, the number of HER sites changes and when that of Cr change the shell thickness/coverage changes. Both affect the same functional unit: the HER microstructure and its selectivity.

Because both loadings control the same balance, too little Rh means not enough HER sites and too much Rh makes larger metal clusters, leading to potentially more recombination and more back reactions. Also, too little Cr_2O_3 does not suppress back reaction and too much Cr_2O_3 blocks proton transport, increases series resistance which in turn reduces electron transfer efficiency. Thus, both have an optimum where Rh sites are numerous enough, Cr_2O_3 coverage is sufficient but not excessive. That naturally leads to similar-shaped curves.

2.3.1 Is such a system electron-limited or hole-limited? Considering the plots in Fig. 3 and 4, for the IrO_2 series H_2 goes from *ca.* 0.85 to *ca.* 2.05 μmol h^{-1} (≈2.4 × increase) while for the Rh series H_2 goes from *ca.* 0.65 to *ca.* 2.6 μmol h^{-1} (≈4 × increase) and for the Cr_2O_3 series H_2 goes from *ca.* 0.25 to *ca.* 2.6 μmol h^{-1} (≈10 × increase). This means that the system is not primarily "hole-limited". If OER kinetics (holes) were the dominant bottleneck, varying IrO_2 should dominate the gains more than Rh or Cr_2O_3. But IrO_2 gives the smallest leverage. Instead, Rh and especially Cr_2O_3 give the strongest leverage. That points toward either electron-side limitations and/or parasitic electron consumption (back reaction/ORR).

Now considering the O_2/H_2 ratio behavior, IrO_2 variation leads to O_2/H_2 rise toward *ca.* 0.5 as IrO_2 increases. Therefore, adding IrO_2 improves hole extraction and OER kinetics, so O_2 catches up. This means that while the hole-side is not perfect, it is fixable and doesn't show threshold behavior. However, Rh variation does not affect the O_2/H_2, it stays around 0.45–0.55 across the whole range. In other words, varying Rh mostly changes how fast electrons make H_2, but it doesn't dramatically change stoichiometric balance. That suggests Rh is mainly affecting HER kinetics/electron transfer, not selectivity. In the case of Cr_2O_3 variation O_2/H_2 is nearly 0 at low Cr, then suddenly jumps to near 0.5 above 1 wt%. Below a certain Cr_2O_3 coverage, O_2 is being lost (reduced away or recombined) and above a coverage threshold, the back reaction is suppressed and the system becomes stoichiometric. The primary limitation is interfacial selectivity/back reaction suppression. That means at low Cr_2O_3, holes and electrons are generated, but the net O_2 is destroyed at/near HER sites. This is not a bulk limitation it is a surface kinetic/selectivity loss. There is a secondary limitation: electron-side kinetics/HER site density. This is because changing Rh causes large increases in H_2 rate and O_2/H_2 stays close to 0.5 (the system remains balanced while rates increase). Still, hole-side kinetics (OER): IrO_2 still matters, it improves O_2/H_2 toward stoichiometric and increases rates but the smaller leverage compared to Rh/Cr suggests OER kinetics are not the main bottleneck once the interface is engineered.

Overall, there are two regimes. Regime A: back-reaction limited (low Cr_2O_3) O_2/H_2 far below 0.5, because O_2 is lost and regime B: kinetics/transport limited (high Cr_2O_3, near-optimal Rh/IrO_2) where O_2/H_2 is about 0.5 and the limiting factors are carrier transport to surface, HER/OER surface kinetics, and light absorption.

In summary of this section, the cocatalyst-loading suggests that performance is primarily limited by interfacial selectivity. In particular, varying Cr_2O_3 produces a threshold-like transition from negligible O_2 evolution ($O_2/H_2 \approx 0$) to near-stoichiometric overall splitting ($O_2/H_2 \approx 0.5$), consistent with suppression of back reactions (*e.g.*, O_2 reduction and H_2/O_2 recombination) once a sufficiently continuous Cr_2O_3 protection layer forms on HER sites. After selectivity is established, the overall rate becomes more sensitive to HER cocatalyst loading (Rh), while OER cocatalyst loading (IrO_2) provides smaller but measurable improvements, indicating that electron extraction/HER kinetics remain the dominant secondary limitation under optimized conditions.

2.3.2 Band-tail states: shallow *versus* deep defect states and their role in photocatalytic performance. It is important to distinguish between shallow band-tail states and deep-level defect states, as they exert markedly different effects on photocatalytic performance. Shallow band-tail states (Urbach tails, typically within 100–150 meV of the band edges) arise from structural and compositional disorder—in oxychalcogenides specifically from mixed-anion (O^{2-}/S^{2-}) distribution, stacking faults, and local strain around coordination polyhedra. Carriers trapped in shallow tail states retain significant thermal energy and can be re-excited into the band within picoseconds to nanoseconds. This suppresses direct band-to-band recombination, extends apparent carrier lifetimes, and creates a potential-fluctuation landscape that spatially separates electrons and holes. This is beneficial for photocatalysis when interfacial selectivity is controlled. Deep-level defect states (typically more than 200–300 meV from the band edges),

by contrast, arise from stoichiometric defects such as sulfur vacancies or grain boundary states. These act as efficient Shockley-Read-Hall (SRH) recombination centers: carriers trapped at deep levels lose energy non-radiatively before reaching the surface, pin the quasi-Fermi levels, and can serve as nucleation points for photocorrosion by concentrating holes on sulfide sites. Notably, band-tail states are not unique to oxysulfides but are a general feature of all mixed-anion semiconductors (*e.g.*, oxynitrides, oxyfluorides, mixed-halide perovskites). What distinguishes oxysulfides is the large anion size mismatch (O^{2-}: 1.40 Å *vs.* S^{2-}: 1.84 Å), producing comparatively strong potential fluctuations at nominal stoichiometry. Intentional engineering of band-tail depth is achievable through: (a) improving long-range anion ordering *via* extended annealing or topotactic synthesis; (b) partial isovalent anion substitution (*e.g.*, $S^{2-} \rightarrow Se^{2-}$) to reduce size mismatch; and (c) epitaxial strain engineering to lock in a specific polar distortion while minimising random disorder.

Further studies revealed that $Y_2Ti_2O_5S_2$ may possess band-tail states that enhance carrier lifetimes and promote photocatalytic activity.[28] As indicated above band-tail states are shallow, exponentially decaying electronic states that extend into the band gap from the conduction or valence band edges. They arise due to any phenomenon that causes small, local variations in the crystal potential. These are due to structural disorder (in this case they are in particular mixed-anion disorder (O^{2-}/S^{2-} distribution) and layered stacking imperfections) and compositional disorder (even if the stoichiometry is nominally $Y_2Ti_2O_5S_2$, slight variations in local S/O ratio or the arrangement of anions create band-edge fluctuations). Other factors include static strain such as local distortions around TiO_5S octahedra/pyramids and layered/sheeted structural motifs.

It has been proposed that these tail states can be beneficial for photocatalysis because of the following.

(a) Improved carrier lifetimes (tail states act as a "buffer zone" between the conduction band and deep trap states).

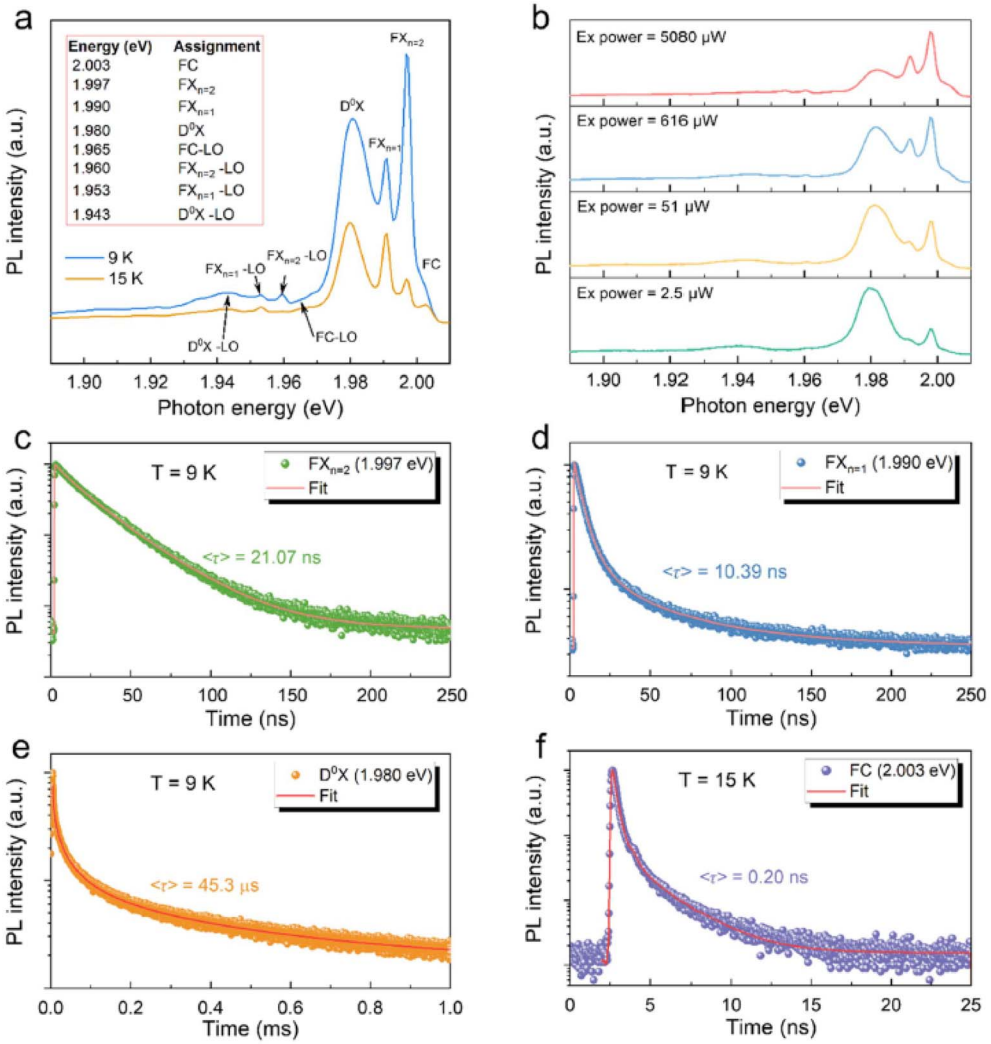

Fig. 5 Low-temperature photoluminescence (PL) spectra and plots of $Y_2Ti_2O_5S_2$ powder. (a) PL spectra of $Y_2Ti_2O_5S_2$ measured at 420 nm laser excitation (9 and 15 K). Peak assignments are shown in the inset. (b) Excitation (E_x) power-dependent PL spectra of $Y_2Ti_2O_5S_2$ at 9 K. (c–e) TRPL decay curves of the $FX_{n=2}$, $FX_{n=1}$, and D^0X peaks at 9 K. (f) TRPL decay curve of the FC peak at 15 K. The red lines in (c–f) are the fitted curves using the thermalized stretching exponential decay, eqn (6). Reproduced from ref. 28 with permission from [The Royal Society of Chemistry] [2026].

Therefore, electrons may fall into a tail state (shallow) then thermally re-excite rather than immediately recombine. This suppresses Shockley-Read-Hall (SRH) recombination.

(b) Enhanced visible-light absorption (reduce the effective band gap for absorption, allowing absorption of lower-energy photons.

(c) Because of (a) there is a better charge separation (tail states can act as stepping stones for electrons or holes to migrate without falling into deep traps).

Fig. 5 presents one of the key results obtained by time resolved photoluminescence of $Y_2Ti_2O_5S_2$. Fig. 5a shows the PL spectra of $Y_2Ti_2O_5S_2$ measured at 9 and 15 K. The main four distinct peaks in the range of 1.97 to 2.01 eV are distinguished by changing the excitation power (Fig. 5b). These four peaks are attributed to free excitons ($FX_{n=1}$ and $FX_{n=2}$), free carrier (FC) and bound exciton (D^0X). The relative intensities of the free excitons peaks at 1.997 and 1.990 eV increase with increasing excitation power, whereas that of the bond exciton at 1.980 eV decreases with increasing excitation power. The decay curves fitted using the thermalized stretching exponential function, eqn (6), are shown in Fig. 5(c-f), from which the average lifetime, $\langle t \rangle$, is extracted.

$$I = I_1 \exp\left(\frac{-t}{\tau_1}\right) + I_2 \exp\left(\frac{-t}{\tau_2}\right)^{\beta} \quad (6)$$

The first term refers to a decay channel with a single characteristic lifetime, often used for a radiative free-exciton recombination or a fast channel that is close to first-order kinetics (no strong distribution of environments). The second term refers to when the decay is stretched, with $\beta < 1$. This is attributed to a broader distribution of recombination environments (different trap depths, local potentials, spatial separation, disorder, diffusion-limited capture, *etc.*). These may be lumped together as bound excitons.

From the fit using eqn (6), $\langle \tau \rangle$ is computed using the Euler gamma function expression.

$$\langle \tau_i \rangle = \frac{\tau_i}{\beta} \Gamma\left(\frac{1}{\beta}\right) \quad (7)$$

The most important observation is the very long $\langle \tau \rangle$ of D^0X. The fact that its intensity decreases with light intensity and without shifting in energy is taken as further indication that it results indeed from a bound exciton. Further TRPL as a function of temperature indicated that D^0X disappears by 60 K with FC becoming the dominant feature up to 300 K. However, it was found that FC have a high activation energy, 92 meV (much higher than room temperature, 25 meV). Based on this and other computation results (DFT-HF (HSE06)) the following interpretation (Fig. 6) is given in which anti-sites of O_S and S_O are the cause. These while neutral since both anions have the same charge, −2, still make fluctuation because (as indicated above) of slight changes in bond distance and associated different electronic structures. While in an ideal semiconductor the conduction band and valence edges are flat and therefore electrons see the same bandgap everywhere, in real materials

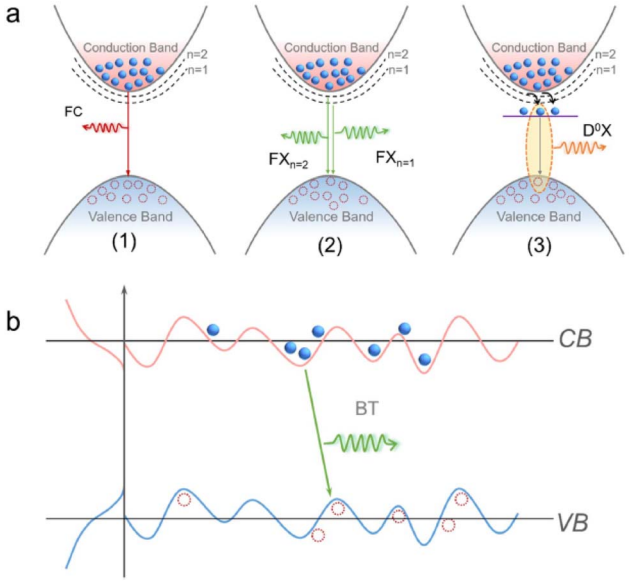

Fig. 6 Schematic diagrams of PL mechanisms in $Y_2Ti_2O_5S_2$. (a) Recombinative emission channels at low temperature: (1) free carrier (FC) recombination, (2) free excitons ($FX_{n=1}$, $FX_{n=2}$) recombination, (3) bound excitons recombination (exciton bound to donor, D^0X). (b) Band structure and emission mechanism of the band-tail transition at 300 K. Reproduced from ref. 28 with permission from [The Royal Society of Chemistry] [2026].

small compositional or structural variations cause the local band edges to shift slightly from place to place. That spatial variation is what is called "potential fluctuations" and this produces band-tail states: states extending into the gap from the band edges. This in turn reduces electron–hole overlap and creates potential barriers for recombination, so recombination becomes slower.

However, these are a double-edge sword, because while moderate band tails increase the lifetime which is good for photocatalysis, too strong band tails would prevent carrier transport and consequently decrease catalytic activity. This is precisely what is found where the activation energy of 92 meV is too high for room temperature reactions under photon excitation. In other words, it was found that the potential fluctuation amplitude is already somewhat large in this material.

One may re-view this upon analyzing the O_2 to H_2 ratios and reaction rates as plotted in Fig. 3 and 4. Band-tail states help charge separation but they also make "inappropriate surfaces" more damaging. Band-tail states (Urbach tails/potential fluctuations) do two main things: increase apparent carrier lifetime, by spatially separating electrons and holes (reduced overlap) and create a landscape of localized carriers. Carriers can be trapped/shuttled through shallow states before reaching the surface. That's good if surface reactions are selective and fast. But longer-lived electrons at/near the surface dramatically increase the probability of undesired reactions (especially O_2 reduction) unless the surface is engineered to prevent them. So tail states don't automatically improve overall splitting. They can actually magnify the importance of surface selectivity. At low Cr_2O_3 ($O_2/H_2 \sim 0$), if electrons survive longer (tail states,

slower recombination), then in pure water they have time to do undesired reactions such as reduce dissolved O_2 and drive back reaction pathways. Above the Cr_2O_3 threshold (O_2/H_2 is *ca.* 0.5), because it suppresses O_2 access to electron-rich HER sites, ORR-type back reaction on Rh and H_2/O_2 recombination, the longer lifetime provided by tail states becomes beneficial rather than harmful: electrons can actually make H_2 and holes can make O_2. In short, bulk lifetime improvement is only useful when interfacial selectivity is controlled.

2.3.3 A key conceptual framework: bulk-limited *vs.* interface-limited regimes. An oxysulfide like $Y_2Ti_2O_5S_2$ appears operating in two regimes.

1. Interface-limited: bulk carriers may live long (tail states), surface pathways are leaky (back reactions, ORR, recombination on metals) and the net overall splitting is poor without adding Cr_2O_3 shells, or using a Z-scheme for spatial separation of HER/OER sites.

2. Bulk-limited: absorption fraction, carriers diffusion length, carries bulk recombination and carrier mobility (too strong tailing can hinder transport). This may be fixed by reducing potential fluctuation amplitude, improve crystallinity, reduce deep traps. Too much band tailing" can reduce STH even if lifetime is long because strong tailing leads to carriers become localized slowing charge transport. This means that long TRPL lifetimes can also be associated with low photocatalytic rates. This is because a long lifetime is only helpful if carriers can reach the reactive sites in time and with the right selectivity.

The use of sacrificial-agent systems distort this picture. In sacrificial systems: electrons (or holes) are rapidly consumed, back reaction is suppressed; long lifetime almost always looks beneficial. So sacrificial tests can incorrectly suggest that: "tail states are unconditionally good" but in pure water tail states can increase the time window for undesired surface chemistry unless selectivity barriers (Cr_2O_3, Z-scheme) are engineered.

In summary of this section, band-tail states and potential fluctuations can extend carrier lifetimes by reducing electron–hole overlap, but their net effect on overall water splitting depends critically on interfacial selectivity. In pure-water systems, long-lived electrons increase the probability of side reactions such as oxygen reduction and H_2/O_2 back reactions unless HER and OER sites are isolated (*e.g.*, *via* Cr_2O_3 shells, spatially separated cocatalysts, or Z-scheme architectures). Consequently, improvements in bulk lifetime (as inferred from TRPL) do not necessarily translate into higher STH efficiencies unless surface recombination and back reactions are simultaneously suppressed. This interplay helps explain why stoichiometric gas evolution ($O_2/H_2 \approx 0.5$) often emerges only beyond a threshold cocatalyst/protection loading, after which bulk transport and absorption become the dominant constraints (Table 3).

Subsequent studies involving sequential loading of cocatalysts and Z-scheme coupling with $BiVO_4$, resulted in an improved STH efficiency of $Y_2Ti_2O_5S_2$-based systems of about 0.19%.[26] Other oxysulfides include $La_5Ti_2AgS_5O_7$ were also found to be active in a powder-suspension Z-scheme systems

Table 3 Consolidated photocatalytic performance of oxy-sulfide systems for overall water splitting in pure water. AQY = apparent quantum yield; STH = solar-to-hydrogen efficiency; N/A = not reported in original reference. Data illustrate the current gap between achieved STH values and the ~10% viability threshold

Material/Cocatalysts	Light source	Conditions	H_2 rate	O_2/H_2	AQY (%)	STH (%)	Stability (h)	Ref.
$Y_2Ti_2O_5S_2$/IrO_2, Rh, Cr_2O_3	$\lambda > 420$ nm, 300 W Xe	Pure water, La_2O_3, pH 8.5	37.5 μmol g^{-1} h^{-1}	~0.5	N/A	0.007	20	[22]
$Y_2Ti_2O_5S_2$ + $BiVO_4$ Z-scheme	$\lambda > 420$ nm, 300 W Xe	Pure water	55 μmol g^{-1} h^{-1}	~0.5	N/A	0.19	N/A	[29]
$La_5Ti_2AgS_5O_7$/Z-scheme	$\lambda > 420$ nm	Pure water	N/A	~0.5	0.12 at 420 nm	0.003	N/A	[30]
$Sr_3In_4O_4S_5$ (SIOS)	Full spectrum	Pure water	Trace	~0.4	N/A	~0.001	N/A	[36]
Acid-treated SIOS (HSIOS)	Full spectrum	Pure water	Low	<0.1 after 4h	N/A	N/A	~5 h	[36]

with 0.12% apparent quantum yield (AQY) at a 420 nm light excitation, and a low STH (0.003%).[30]

It is also important to place these efficiencies in context. For particulate photocatalyst systems operating in pure water, several intrinsic loss channels, including incomplete light absorption, carrier recombination, back reactions, and mass-transport limitations, reduce the achievable STH efficiency well below the thermodynamic limit. In practice, achieving STH values above 5–10% in suspended photocatalyst systems remains elusive. The fact that most oxysulfide systems currently operate at STH values below 1% indicates that substantial improvements in carrier lifetime, surface reaction kinetics, and light-harvesting efficiency are still required before practical implementation becomes feasible.

A key observation across many studies is that improvements in crystallinity, cocatalyst dispersion, and heterojunction design often lead to incremental gains in activity but do not yet translate into order-of-magnitude increases in efficiency. This suggests that intrinsic limitations—such as carrier diffusion length, bulk recombination, and imperfect band-edge alignment—are likely to play a dominant role. Consequently, future progress requires simultaneous optimization of bulk electronic structure and interfacial charge transfer rather than further incremental modifications alone.

2.4. The synergic strategy of oxygen and sulfur in oxy-sulfides

The improved performance of oxy-sulfides is linked to anion driven electronic modulation because of higher polarizability of sulfur ($\alpha \approx 7$ Å^3 for S^{2-} compared to ≈ 3.0 Å^3 for O^{2-}). This increased polarizability leads to a stronger covalency with transition metal cations, like Ti^{4+}. As indicated above, this increased covalency, in turn, leads to the valence band maximum being pushed higher with S 3p and O 2p hybridization. Consequently, the hybridization reduces the bandgap. For example, from ~3.2 eV to ~1.9 eV when comparing $Y_2Ti_2O_7$ to $Y_2Ti_2O_5S_2$. The conduction band is still sufficiently negative for H^+ reduction.

In attempt to further understand such a system a computational study pointed out that due to the lower electronegativity of sulfur, sulfides normally have band gaps that are too small for water splitting but polar distortions could shift their band gap to a suitable range. These polar distortions, made by either epitaxial strain or substitution of sulfur by oxygen, increase the band gap to a suitable range. As an example, the compressively strained $BaZr_{1-}YTiYO_2S$ compounds were proposed as photocatalytic water splitting.[16,27,31] The valence band maximum is governed by anion stoichiometry. An excess of S destabilizes the lattice. Calculations suggest that about a 50% S fraction yields a near ideal band gap of about 2.0 eV and with thermodynamic stability. Local strains introduced upon replacing O^{2-} by S^{2-} induces tensile strain in MO_6 or MS_6 octahedra. This destabilizes the VBM and increases absorption of visible light (upward shift by 0.4 to 0.7 eV). Polar distortions arise when mixed O and S environments break inversion symmetry (as indicated above). When the cations on the B site (*e.g.*, Ti^{4+} in TiO_5S_1 units), shift from the center of the polyhedron and are correlated across the lattice, as in layered perovskite-type oxysulfides, a macroscopic spontaneous polarization of approximately 10–15 μC cm^{-2} is generated.[16] This built-

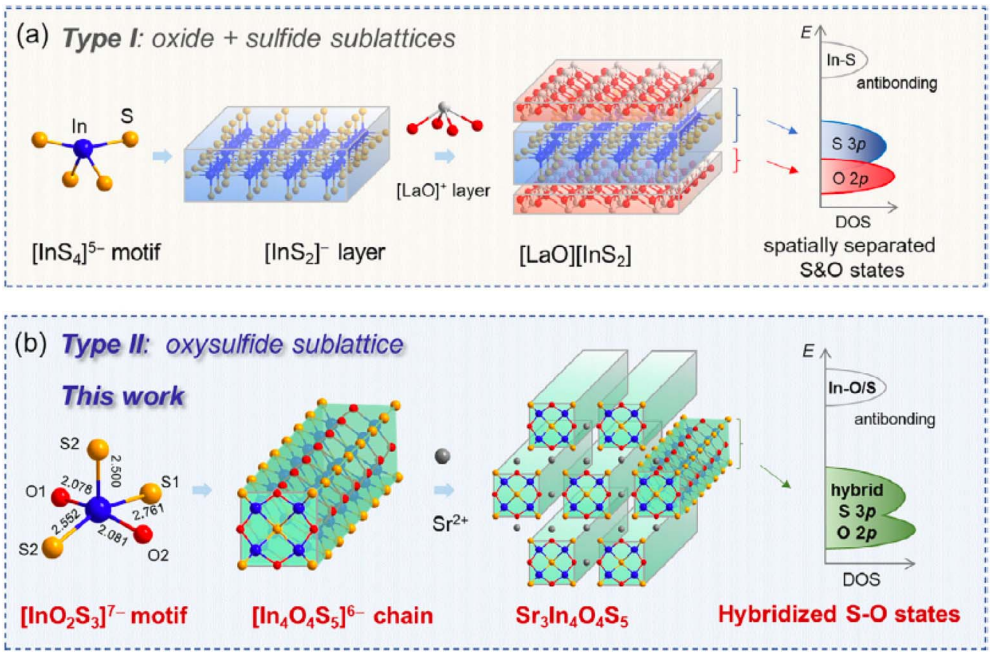

Fig. 7 Two types of oxysulfides. (a) Type I: oxysulfides constructed from oxide and sulfide sublattices. In the scheme $LaOInS_2$ has a layered structure composed of alternating $[LaO]^+$ and $[InS_2]^-$ layers. This results in "largely" a spatial separation of O and S states. (b) Type II: oxysulfides containing hetero-anionic sublattices. $Sr_3In_4O_4S_5$ (SIOS) has a one-dimensional structure containing $[InO_2S_3]^{7-}$ square pyramids. This results in hybridized S–O state near the Fermi level. Reproduced from ref. 36 with permission from [John Wiley and Sons, License Number 6211401230882] [2026].

in electric charge surface density acts as an internal charge-separation driving force: photogenerated electrons and holes are swept in opposite directions, reducing their spatial overlap and suppressing SRH recombination. Experimental evidence comes from TRPL measurements of $Y_2Ti_2O_5S_2$ (Fig. 5), where the stretched-exponential decay and high activation energy (92 meV) for free-carrier recombination are consistent with spatially separated carriers navigating the potential-fluctuation landscape induced by mixed-anion disorder.

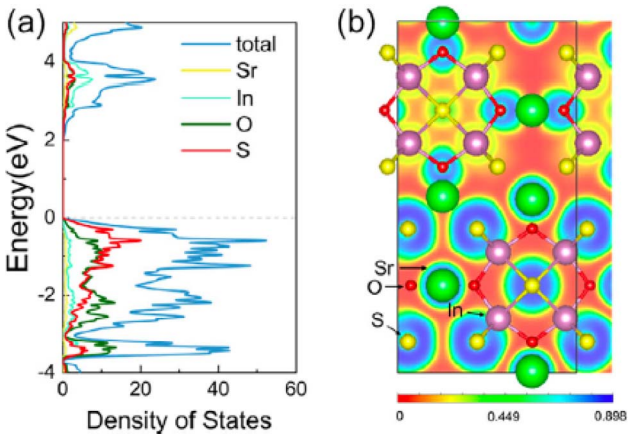

Fig. 8 The electronic structure of $Sr_3In_4O_4S_5$ and bonding of the In-centered hetero-anionic motif. (a) Total and partial Density of States (DOS) of elements of $Sr_3In_4O_4S_5$. (b) Valence electron density map projected on the (001) plane located at $z = 0.25$. Reproduced from ref. 36 with permission from [John Wiley and Sons, License Number 6211401230882] [2026].

2.5. Oxysulfide semiconductors with hetero-anionic units $[O–In–S]^{x-}$, $Sr_3In_4O_4S_5$

Indium-based oxysulfides materials such as $LaInOS_2$,[32] $La_5In_3S_9O_3$,[33] and $La_{10}In_6S_{17}O_6$ (ref. 34,35)), have been reported. These do not contain hetero-anionic coordination around the In cation and are therefore made of separated oxide and sulfide sub-lattices. This results in spatially O and S states and therefore show weak orbital hybridization (Fig. 7a). Recently, a quaternary indium oxysulfide, $Sr_3In_4O_4S_5$ (SIOS), constructed from hetero-anionic $[InO_2S_3]^{7-}$ units has been recently synthesized and tested for the water splitting reaction.[36] This hetero-anionic sub-structure allows for closer spatial atomic mixing of S and O (hybridization) (Fig. 7b). Therefore, it added other dimensions to the oxysulfides function making them tunable platforms ion which anion distribution, strain, and symmetry breaking may act as independent design parameters.

Fig. 8a presents the density of states as computed using density functional theory (DFT) within the generalized gradient approximation (GGA), where the VB maximum is composed of S 3p and O 2p orbitals while the CB minimum derives from the empty In 5s orbitals. The valence electron density map (Fig. 8b) indicates high electron density around S and O atoms. The extracted band gap energy is found to be 3.2 eV. HRTEM images and selected area electron diffraction pattern reveal that one of

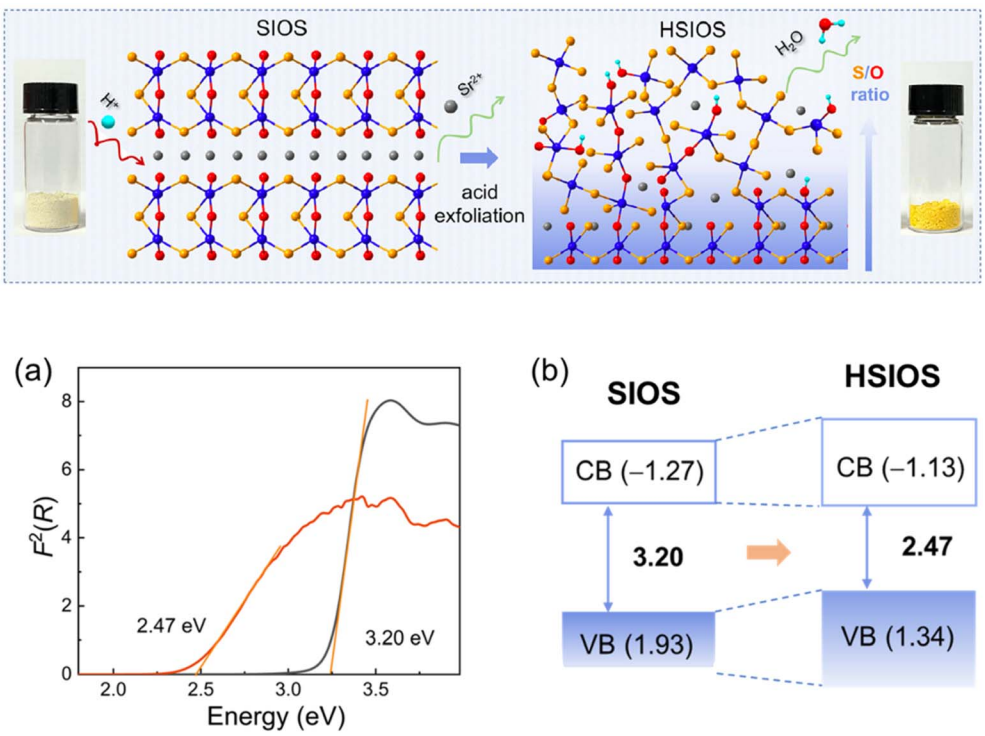

Fig. 9 (a)Schematic of the structural transformation from pristine SIOS ($Sr_3In_4O_4S_5$) to "acid-treated $Sr_3In_4O_4S_5$ (HSIOS) after topological acid exfoliation. Inset: the image of SIOS and HSIOS samples. (a) Tauc Plots, $F^2(R)$ as a function of energy of SIOS (black) and HSIOS (red). (b) Band energy diagrams of SIOS and HSIOS. Energy levels are with respect to the normal hydrogen electrode (NHE). Reproduced from ref. 36 with permission from [John Wiley and Sons, License Number 6211401230882] [2026].

the exposed crystal faces is the (3,−1,1) face, displaying 1D chains extending along the dominant crystal growth direction. (EDS) analysis confirms the uniform distribution of Sr, In, O, and S; further structural details can be found in (ref. 36).

In order to decrease the bandgap energy, the authors have transformed part of the compound to amorphous (Fig. 9) by acid treatment. The resulting material "acid-treated $Sr_3In_4O_4S_5$ (HSIOS), has resulted in a band gap energy of *ca.* 2.5 eV and with a raised valence band level without much change in the CB position. This made HSIOS more suitable for sun light harvesting. Photocatalytic test results showed however that while SIOS had weak activity for water splitting, the ratio of H_2 to O_2 of 2 was an indication of stability (for some time at the experimental conditions). The ratio H_2/O_2 obtained using the acid treated SIOS (HSIOS) deviated considerably from 2, due to corrosion and is therefore found to be not stable. This, again, is linked to the fact that the creation of "defect, amorphous" states destabilize the material by accelerating undesired reactions in particular corrosion (non-stoichiometric H_2/O_2 ratios).

3 Oxy-sulfides in electrocatalytic hydrogen evolution (HER)

3.1 NiFe oxy-sulfides: a promising earth-abundant electrocatalyst

Oxy-sulfides have also attracted much interest recently as HER electrocatalysts owing to the integration of oxide stability and sulfide conductivity. Of the widely investigated examples are NiFe oxy-sulfides, which are typically synthesized by sulfidation of $NiFe_2O_4$ using H_2S. Selective incorporation of sulfur tunes the sulfur-to-metal ratio and phase composition to yield high HER activity. Optimized structures like NFS_{100}–N_2 and NFS_{300}–H_2 (the subscript represents the temperature of sulfidation, °C, whereas the suffix differentiates the sulfidizing atmosphere, in this case, N_2 = 5% H_2S in N_2, whereas H_2 = 10% H_2S in H_2,[29]) exhibit overpotentials as low as ∼266 mV at −10 mA cm^{-2} and demonstrate stable performance for >10 h. This is an example of key contribution of sulfidation to a marked increase in both electrochemically active surface area and charge transfer efficiency compared to the parent oxide, making NiFe oxy-sulfides, so far, amongst the most active earth-abundant HER catalysts.[37]

A comparison of NiFe oxysulfides with their parent NiFe oxides and NiFe sulfides reveals three specific performance advantages. (i) Electrochemically active surface area (ECSA): partial sulfidation of $NiFe_2O_4$ produces a porous, defect-rich morphology that substantially increases ECSA relative to the parent oxide surface, while avoiding the agglomeration that occurs in fully sulfided phases. (ii) Charge-transfer kinetics: NiFe sulfides exhibit high electronic conductivity but tend toward surface passivation under alkaline conditions *via* formation of insulating sulfate layers, whereas NiFe oxides display slow charge transfer due to their wider band gaps. NiFe oxysulfides maintain partial sulfide character for high conductivity while the residual M–O framework prevents further/deeper reactions, yielding Tafel slopes (∼120 mV dec^{-1}) consistent with a more facile Volmer step. (iii) Mixed-valence active sites: the mixed O/S coordination environment stabilises simultaneously Ni^{2+}/Ni^{3+} and Fe^{2+}/Fe^{3+} oxidation states, providing adjacent Lewis-acidic sites for water adsorption and proximal S sites that act as proton relays, a mixed-valence configuration structurally difficult to achieve in single-anion materials.

The role of sulfur content is further nuanced by *in situ* structural evolution under operating conditions. Low-temperature sulfidation favors a thin oxysulfide shell around the oxide core, preserving structural integrity, whereas high-temperature sulfidation converts more bulk oxide to sulfide, increasing conductivity at the cost of stability. Under cathodic HER conditions in alkaline media, surface oxysulfide phases can partially reconstruct into NiFe oxyhydroxide (NiFeOOH) layer that can be beneficial. This dynamic evolution makes the as-synthesised phase an imperfect descriptor of catalytic performance and highlights the critical need for *operando* XAS and Raman characterisation to identify the true active surface phase, as discussed in Section 5.1.

3.2. Other oxysulfides electrocatalysts

Other than NiFe systems researchers have also incorporated sulfur into oxyhydroxide structures such as CoFeOOH. Sulfur-modified CoFe oxyhydroxide supported on nickel foam exhibits high activity with merely 48 mV required for HER and 186 mV for the OER at 10 mA cm^{-2}. A full electrolyzer from the catalyst exhibited 10 mA cm^{-2} at 1.54 V, outperforming a reference Pt/IrO_2 system.[38]

Other examples include nanostructured tungsten oxysulfides as HER electrocatalysts with enhanced charge transport and catalytic activity. Though performance varies from report to report, studies indicate that incorporation of W enhances the production of hydrogen.[39] Control over anions has also been an effective design strategy, exemplified by NiFe (oxy) sulfides with adjustable oxygen-to-sulfide ratios. One composition, NiFeS-2 (nanoparticles with an average diameter of *ca.* 20 nm together with graphene), had a very low OER overpotential of 286 mV at 10 mA cm^{-2} with a Tafel slope of 56 mV dec^{-1} (Fig. 10).[42]

Finally, mixing oxy-sulfides with conducting phases offers yet another avenue for performance enhancement. $NiFe_2O_4$, for example, in mixture with transition-metal sulfides such as MoS_2 or CoNi–S, forms heterostructures that are more conductive and with more efficient charge transfer across the interface. These have achieved notable improvements in HER and OER activity in alkaline conditions.[41] The electrocatalytic performance data from typical reports are summarized in Table 4, including current densities, Tafel slopes, and overpotentials. The comparison illustrates how compositions of oxy-sulfides and hybrid methods influence HER activity.

A comparison of reported performance values reveals several important trends. First, the overpotentials of oxy-sulfide catalysts generally fall in the range of 200–300 mV at −10 mA cm^{-2}, placing them among competitive earth-abundant catalysts but still above the best transition-metal phosphides, nitrides, and some sulfide systems. Second, improvements in activity are frequently correlated with increased electrical conductivity,

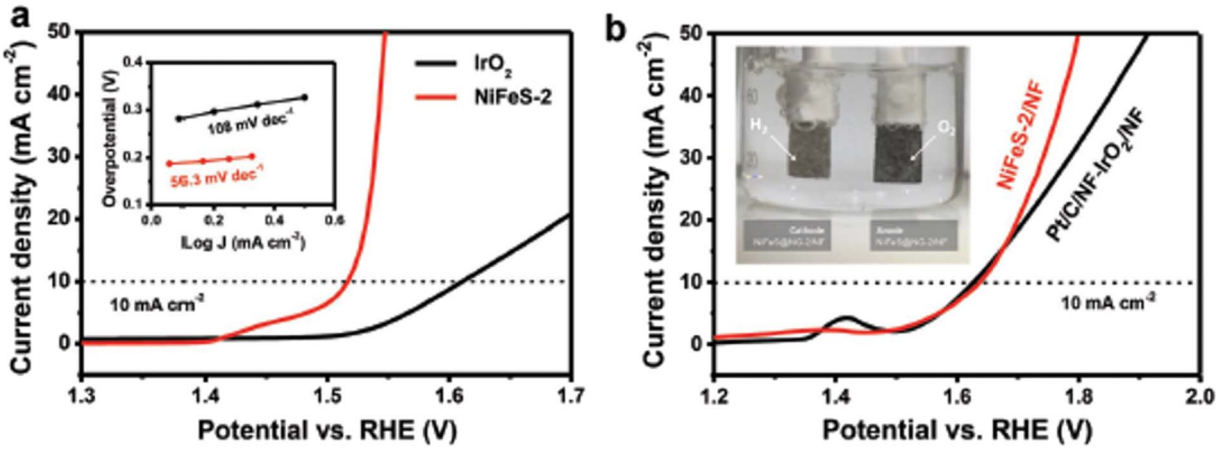

Fig. 10 Electrochemical evaluation of an optimized NiFeS-2 electrocatalyst (has a morphology of NiFeS nanoparticles with an average diameter of *ca.* 20 nm together with graphene) under anionic regulation. (a) OER LSV profiles and inserted Tafel plots of NiFeS-2 and IrO_2 electrocatalysts in O_2-saturated 0.10 m KOH. (b) LSV profiles and inserted picture of NiFeS-2/NF and Pt/C–IrO_2/NF electrocatalyst for overall water splitting in N_2-saturated 1.0 m KOH; NF: nickel foam. Reproduced from ref. 42 with permission from [John Wiley & Sons, License Number 6215221463062] [2026].

Table 4 Electrocatalytic performance of some oxy-sulfide catalysts for the HER, with focus on exchange current density, Tafel slope, and overpotential at −10 mA cm^{-2}. To put in context, typical performance of HER catalysts is as follow @10 mA cm^{-2}: Pt: ∼30–50 mV, NiMo or NiFe alloys: ∼50–100 mV, many sulfides: 150–250 mV

Catalyst	Exchange current density (mA cm^{-2})	Tafel slope (mV dec^{-1})	Overpotential (mV) at 10 mA cm^{-2}	References
NiFe oxy-sulfide (NFS100–N_2, NFS300–H_2)	∼0.15	≈120	≈266	[37]
S-incorporated CoFe oxyhydroxide on Ni foam	∼0.30	≈52	≈48	[38]
Nanostructured tungsten oxysulfide	N/A	N/A	≈200–300	[39]
NiFe (oxy)Sulfide (NiFeS-2, anion-regulated)	∼0.12	≈56	≈286 (OER focus)	[42]
$NiFe_2O_4$-based heterostructure (with MoS_2 or CoNi–S)	N/A	≈110	≈300–350	[41]

higher electrochemically active surface area, and the formation of mixed-valence metal sites during operation. Third, heterostructure formation and anion regulation appear to be more effective strategies than simple compositional modification, as they directly influence charge transfer pathways and catalytic site availability.

These observations suggest that the principal role of oxy-sulfides in electrocatalysis may not be to achieve record-low overpotentials, but rather to provide catalysts that balance activity, stability, and compositional tunability, properties that are particularly important for long-term alkaline electrolysis.

Despite these the stability of many oxy-sulfide catalysts is still limited by surface reconstruction and gradual sulfur loss, particularly under extended operation or high current densities. In many systems, the catalytically active phase evolves during operation into mixed oxyhydroxide or sulfide-derived layers, making it difficult to identify the true active species. Furthermore, improvements in intrinsic activity have often been accompanied by increases in catalyst complexity, including multistep synthesis routes or reliance on conductive supports, which may complicate large-scale implementation. These considerations suggest that future progress will require greater emphasis on understanding *operando* structural evolution and designing materials whose active states are both stable and well-defined.

Overall, oxy-sulfides occupy an intermediate position between oxides and sulfides in electrocatalysis: they rarely outperform the most active sulfide-based catalysts in terms of intrinsic activity, but they often provide improved structural robustness and greater compositional flexibility. This balance of properties may ultimately prove more important for practical electrolyzer operation than achieving the lowest possible overpotential under laboratory conditions.

4. Challenges, limitations, and deactivation mechanisms

Catalysts deactivation is an unavoidable process and is one of the main limiting factors for the long-term use of water-splitting technologies. Oxy-sulfides are more complicated because they pair two anions with distinct chemistries: oxygen is likely to stabilize shapes and withstand oxidative attack, while sulfur increases light absorption and electronic conductivity but is more easily lost under reactive conditions. These mutually

conflicting tendencies produce a broad spectrum of potential failure modes (surface reconstruction, ion leaching, phase conversion, photocorrosion, and binder failure, among others) all can evolve in parallel under working conditions, making stability a systems-level property rather than a single-material characteristic.[43,44]

While these degradation pathways are well documented, it is important to distinguish between failure mechanisms that are intrinsic to mixed-anion materials and those that are common to most transition-metal chalcogenides. In oxy-sulfides, the simultaneous presence of oxygen and sulfur introduces additional thermodynamic and kinetic complexity, including anion redistribution, selective sulfur oxidation, and strain-driven phase segregation. As a result, stability is governed not only by surface chemistry but also by bulk anion ordering and lattice energetics, making degradation processes inherently multiscale.

1. One of the most frequently encountered changes for transition-metal sulfides in HER (and related cathodic/photocatalytic reactions) are surface triggered conversion:

Crystalline sulfide → amorphous hydroxy/oxy-sulfide intermediate → oxide

Operando analysis indicated that this occurs on timescales varied from minutes to hours and is accelerated by coupled proton/electron transfer, pH shift in localized areas, and contact with dissolved oxygen molecules or hydroxides.[45] Other studies showed that surface triggered conversion occurs when transition metal sulfides are in contact with water/or and dissolved oxygen. Local pH shifts and coupled proton and electron transfer have driven the formation of oxy-sulfide or hydroxy-sulfide layers.[46] These layers were formed in practical timescales during steady operation. The converted oxy-sulfide or mixed oxide sulfide surfaces becomes the working surface because it is more stable than the pristine sulfides under real conditions. It also provides active sites that support charge transfer and bond breaking during catalytic reactions. This means the transformation can improve function when it is guided and controlled.[34,47,48] The goal is to create stable and active oxy-sulfide surfaces through routes such as preformation of oxy-sulfide films, controlled oxidation, doping, or surface modification.[37,49]

2. Electrochemical dissolution leading to compositional exchange is another critical degradation pathway. Under applied potential, transition metals can dissolve from the catalyst lattice, and the rate of this dissolution is fundamentally governed by two material properties: (i) the cohesive energy of the metal and (ii) its oxide affinity – tendency to be oxidized.[50] Metals with low cohesive energy (*e.g.*, Co, Ni) are more easily leached, while those with high oxide affinity (*e.g.*, Ti, Zr) tend to form stable surface oxides that may passivate or block active sites. This leads to compositional drift—either through loss of active species (leaching) or uptake of electrolyte cations (*e.g.*, K^+, Na+) until a new quasi-equilibrium surface/subsurface layer forms.[50] Quantitative online techniques such as inductively coupled plasma mass spectrometry (ICP-MS) and *operando* X-ray absorption/emission spectroscopy (XAS/XES) have quantified this loss channel even under cathodic conditions, revealing that dissolution is a thermodynamically driven process under potential control.[46] Stabilization strategies include lattice doping (to strengthen metal–anion bonds), sacrificial protective layers (*e.g.*, ultrathin Al_2O_3 layer) and the addition of low-solubility cations (*e.g.*, La^{3+}, Y^{3+}) that suppress leaching by occupying surface sites or forming insoluble secondary phases.[44]

3. Photocorrosion and photoinduced degradation also occur in sulfide photocatalysts. Here, photogenerated holes or reactive oxygen species oxidize S^{2-} to surface sulfates or soluble sulfur species with resultant elemental loss and electronic disturbance. There are large bodies of literature on CdS, CuS, and other chalcogenides that document these mechanisms and find protection in the form of heterojunctions, cocatalyst shuttles, thin layer oxide overlayers, and Z-scheme architectures that redirect photogenerated holes away from vulnerable sulfide sites.[40,51,52]

4. Surface reconstruction and active-site evolution are also central to transition-metal chalcogenide activity. Some of these catalysts are reconstructed under working conditions, giving rise to mixed oxide/sulfide domains or vacancies-rich materials. Such reconstructed motifs may result in active catalytic states but may also evolve into unstable structures. *Operando* microscopy and spectroscopy experiments reveal that sulfur migration, vacancy formation, and associated changes in oxidation states have critical effects on both activity and stability. Engineering the kinematics of such processes by way of methods such as carbon encapsulation or controlling vacancy has shown improved catalytic materials.[48,53]

Mechanistically, transition metal sulfides form oxysulfide interlayers in aqueous environments through three interconnected processes. First, surface S^{2-} is thermodynamically unstable in the presence of water and dissolved oxygen: it is oxidised to SO_4^{2-} or S^0 and lost from the lattice, with the resulting vacancies immediately filled by OH^- or O^{2-} from the electrolyte, forming a mixed O/S surface layer. This process is spontaneous because the M–O bond (higher lattice energy) is thermodynamically preferred over M–S under oxidizing or neutral aqueous conditions. Second, during HER or photocatalytic water reduction, coupled proton and electron transfer shifts the local metal oxidation state, making adjacent S^{2-} sites more susceptible to substitution by OH^-; *operando* studies confirm this occurs on timescales of minutes to hours under steady-state cathodic conditions.[45–47] Third, in layered or nanostructured sulfides the weakly ionic interlayer spacings allow facile anion diffusion: O^{2-} and OH^-, being smaller and more strongly hydrated than S^{2-}, penetrate these spacings with low activation energy, creating an oxysulfide interlayer that is more stable, hydrophilic, and often more catalytically active than the pristine sulfide surface. Further reconstruction into oxyhydroxide phases is driven by:

(i) Continued selective S^{2-} oxidation;

(ii) Topotactic OH^- insertion displacing S^{2-} to form M–OOH;

Table 5 Causes of degradation mechanisms, their timescale and possible mitigation solutions

Degradation mechanism	Typical cause	Timescale	Mitigation
Photocorrosion	Hole oxidation of S^{2-}	hours	Cocatalysts, coatings
Surface reconstruction	Potential, pH	Minutes–hours	Controlled pre-oxidation
Cation dissolution	Electrochemical potential	Hours–days	Doping, stabilization
Binder degradation	Electrolyte exposure	Hours–days	Binder-free electrodes

(iii) Thermodynamic preference for oxyhydroxide phases at high local pH and under cathodic potential; and

(iv) Kinetic facilitation by structural disorder in the mixed-anion material. Crucially, the reconstructed oxyhydroxide surface may itself be catalytically active: in NiFe and CoFe systems the evolved NiOOH or FeOOH layer is often the true active phase, making *operando* identification of the working surface phase essential.

From points 1 to 4, three degradation mechanisms appear to dominate the long-term behavior of oxy-sulfide catalysts:

(i) Sulfur loss through oxidation or dissolution, a deeper mechanistic analysis of these three pathways is warranted. For sulfur loss, we distinguish: (i) oxidative S^{2-} dissolution, dominant under photocatalytic and anodic conditions as photogenerated holes or dissolved O_2 oxidise surface sulfide to soluble sulfate; (ii) reductive de-sulfurisation under strongly cathodic alkaline conditions; and (iii) bulk diffusion-driven S redistribution at elevated temperatures. For surface reconstruction, the thermodynamic driving force is the greater drive for of M–O bonds relative to M–S in aqueous environments, compounded by local pH gradients at the catalyst surface. The critical practical distinction is between beneficial reconstruction (yielding a stable, catalytically active oxyhydroxide layer) and detrimental reconstruction (yielding an insulating oxide passivation layer blocking active sites). For compositional drift, ICP-MS measurements have quantified Ni and Fe dissolution rates of 1–10 ng cm^{-2} s^{-1} even under cathodic potentials, cumulatively altering surface stoichiometry on hour timescales. The thermodynamics and kinetics of photocorrosion in sulfide-based photocatalysts and available protective strategies have been reviewed comprehensively in the context of chalcogenide systems.[54]

5. Finally, electrode structure and binder stability play a non-trivial role. Polymer binders used for electrode preparation may block pores, limit active site availability, and chemically degrade upon contact with alkaline, acidic, or irradiated environments, leading to loss of connectivity and structural stability. Binder-free architectures, including direct catalyst growth on conductive supports, three-dimensional scaffolds, and freestanding films, are a few methods addressing this failure and using them has shown better long-term performance.[55,56]

These observations taken together highlight that oxy-sulfides deactivation can be avoided or at least largely retarded using integrative measures. Controlled pre-formation of inert oxy-sulfide surfaces,[37,49] encapsulating ultrathin layers,[45,57] heterostructure engineering and cocatalyst incorporation,[51,53] doping and lattice modification,[47,58] and binder-free electrode architectures[51,55] each targets a unique degradation pathway. Combined, these approaches provide a pathway to survive deactivation as well as to leverage controlled reconstruction to maintain or even enhance catalytic performance under prolonged operation. A fundamental challenge in oxy-sulfide systems is that many of the properties that enhance catalytic activity, such as high covalency, mixed-valence metal sites, and extent of defects, also tend to reduce thermodynamic stability. Consequently, improving activity and durability are often competing objectives. Designing materials that balance these opposing requirements remains one of the central difficulties in the field and explains why many high-activity catalysts still exhibit limited long-term stability.

Looking forward, several research directions appear particularly important. First, *operando* and time-resolved characterization techniques are essential to identify the true active phases and quantify degradation kinetics under realistic operating conditions. Second, greater attention should be paid to bulk anion ordering and defect thermodynamics, as these factors strongly influence both band structure and long-term stability but remain relatively underexplored. Third, strategies that intentionally design catalysts to operate in their reconstructed state, rather than attempting to suppress reconstruction entirely, may provide a more realistic pathway toward durable materials. Finally, achieving stability over thousands of hours under practical current densities or solar fluxes remains a critical benchmark that few oxy-sulfide systems have yet reached.

Many reports evaluate catalyst stability over timescales of only a few hours to tens of hours; however, practical deployment in electrolysers or photocatalytic reactors requires stability over thousands of hours, highlighting a significant gap between laboratory testing and real-world requirements. Table 5, highlights some of the above mentioned causes.

5. Future directions: the way to scalability and real-world applications

Although significant progress has been achieved in understanding and improving oxy-sulfide catalysts, translating laboratory-scale demonstrations into practical hydrogen-production technologies remains a substantial challenge. In particular, three issues will largely determine the future impact of oxy-sulfide systems: (i) improving solar-to-hydrogen efficiency under pure-water conditions, (ii) achieving long-term structural and chemical stability, and (iii) developing scalable synthesis and reactor architectures. Addressing these challenges simultaneously, rather than in isolation, will be essential for real-world deployment.

5.1. Employing advanced research techniques

A key challenge in designing oxy-sulfide catalysts is understanding their dynamic behavior under working conditions. Recent works point to the importance of *in situ* and *operando* techniques *e.g.*, X-ray absorption spectroscopy (XAS),[49] Raman spectroscopy,[53] and transmission electron microscopy to track structure transformation, oxidation state evolution, and active site alteration under working conditions.

At the computational level, merging DFT-based methods with machine learning–based screening makes discovery of stable and efficient compositions more possible. This is done through merging the strengths of each paradigm in explaining intricate catalytic mechanisms and lowering the experimental search space.[59,60]

The application of computational methods, particularly density functional theory (DFT) and its hybrid variants, has been instrumental in rationalizing the electronic structure of oxy-sulfide semiconductors. Standard GGA functionals systematically underestimate band gaps in mixed-anion systems; hybrid functionals (*e.g.*, HSE06) or DFT + U approaches provide more accurate band edge positions. For $Y_2Ti_2O_5S_2$, HSE06 calculations correctly reproduced the experimental band gap of ~1.9 eV and identified O_s/S_o antisite disorder as the structural origin of band-tail states (Section 2.3b). First-principles molecular dynamics (FPMD) models structural evolution of oxysulfide surfaces under aqueous conditions, providing atomistic insight into anion-exchange and reconstruction mechanisms. Machine learning potentials trained on DFT data extend accessible timescales to the microsecond regime. High-throughput DFT screening combining band gap, band edge alignment with redox potentials, thermodynamic stability (convex hull analysis), and defect formation energies offers a powerful route to identify new candidate materials. Key descriptors that machine learning models should target include: band gap and band edge alignment *vs.* H^+/H_2 and H_2O/O_2 redox potentials; anion formation and S/O substitution energies; effective carrier masses and mobility; surface S^{2-} oxidation potential (photocorrosion proxy); Urbach energy as a disorder/band-tail-depth predictor; and M–S bond covalency with d-band centre position as HER activity descriptors. Among *operando* techniques, urgency ranking for oxy-sulfide systems is: (1) XAS/X-ray absorption near-edge structure (XANES), and extended X-ray absorption fine structure (EXAFS)for tracking S^{2-} loss and coordination changes; (2) *operando* Raman for M–S/M–O modes and phase reconstruction; (3) ambient pressure X-ray photoelectron spectroscopy (AP-XPS) for quantitative surface anion composition under near-realistic conditions; (4) time-resolved transient absorption spectroscopy (TAS) for carrier lifetime *vs.* band-tail state occupancy correlation.

Beyond identifying degradation pathways, *operando* techniques will be increasingly important for determining the true active phases, which often differ from the as-synthesized materials. Coupling time-resolved spectroscopy with electrochemical or photocatalytic measurements may enable direct correlation between structural evolution and catalytic performance, providing insights that cannot be obtained from *ex situ* characterization alone. Such understanding will be critical for designing catalysts that remain active in their reconstructed state rather than degrading into inactive phases.

5.2. Engineering for industrial-scale production

Upscaling oxy-sulfide synthesis necessitates processes that keep material quality within affordable expenses. Mechanochemical pathways through ball milling was used for making CdS-based composites with improved H_2 production.[61] Solid state reaction was successfully used to make oxysulfide perovskites such as $Y_2Ti_2O_5S_2$ (ref. 22), it may well be substituted by mechanochemical ball milling, Fig. 11, to scale up the synthesis.

At the reactor scale, Z-scheme heterojunctions, such as Mo(S,O)/Co(O,S) systems showed improved light absorption and charge separation and hence better hydrogen production in

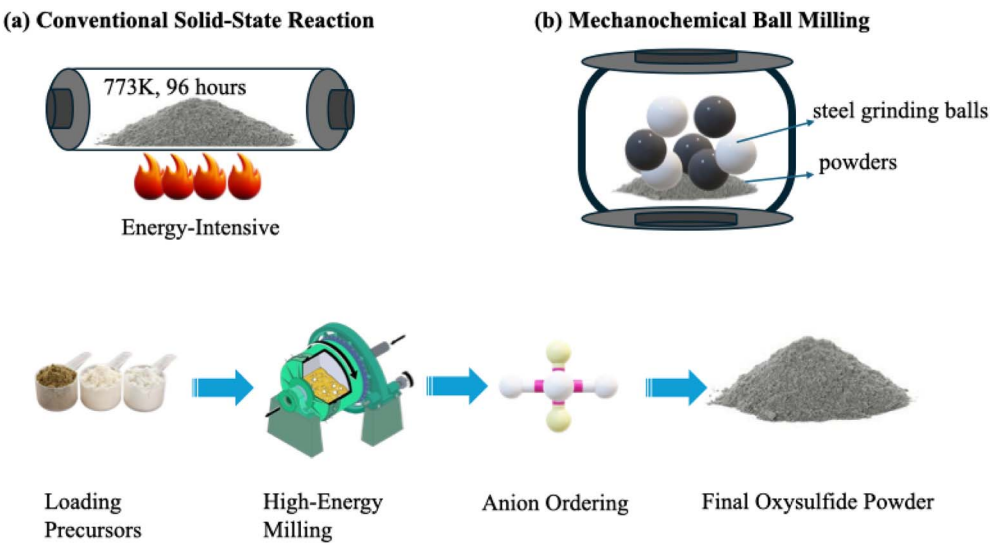

Fig. 11 Schematic illustration for the preparation of oxysulfide perovskites. (a) Conventional solid-state synthesis, and (b) ball milling synthesis.

photocatalysis applications.[62] Up-scaling these concepts into functional photoreactors will be key for field deployment.

Economically, dependency on noble-metal cocatalysts remains a drawback. Novel strategies are aimed at earth-abundant alternatives, *e.g.*, cross-linked MoS_2/WS_2 catalysts that achieve high H_2-evolution rates with low precious-metal loading. While ReS_2 has shown promise as a cocatalyst, rhenium is a scarce and expensive element; thus, its use contradicts the goal of scalable, cost-effective hydrogen production. Future efforts may prioritize truly abundant materials such as Fe-, Co-, Ni-, or Mo-based sulfides and their hybrids.[63,64] In order to realize the full potential of oxy-sulfides, several design handles such as heterojunction construction, defect engineering, cation/anion doping, and cocatalyst loading may be. targeted. Ternary-metal-sulfide/TiO_2 heterojunction overviews highlight how the multi-pronged strategy maximizes carrier separation and light utilization; key lessons for oxy-sulfide development.[65]

From a practical perspective, achieving STH efficiencies above approximately 10% under pure-water conditions remains a widely cited threshold for economic viability. Most known systems currently operate at efficiencies well below this level, indicating that significant improvements in light absorption, charge separation, and catalytic kinetics are still required. Future progress will likely depend on integrated approaches combining optimized band structures, heterojunction architectures, and efficient cocatalysts rather than incremental improvements in any single parameter.

Among the various strategies explored to date, several appear particularly promising. Mixed-anion engineering that enables internal electric fields or polar distortions may enhance carrier separation at the bulk level, while heterostructure design remains one of the most effective methods for suppressing recombination. In addition, defect engineering that introduces shallow states without creating deep recombination centers offers a pathway to improve carrier lifetimes. Finally, designing catalysts that are intrinsically stable in aqueous environments—rather than relying solely on protective coatings—may prove essential for long-term operation.

Scaling oxy-sulfide materials from gram-scale synthesis to kilogram-scale production introduces additional challenges, including maintaining phase purity, controlling anion distribution, and ensuring reproducibility of catalytic performance. Many synthesis methods reported in the literature rely on carefully controlled atmospheres, multi-step processing, or high-temperature treatments that may be difficult to implement at industrial scale. Developing synthesis routes that are both scalable and environmentally benign will therefore be a critical area of future research.

Overall, oxy-sulfides represent a promising yet still emerging class of materials for sustainable hydrogen production. Their unique combination of tunable electronic structure, visible-light activity, and improved stability relative to pure sulfides offers significant opportunities, but substantial challenges remain in efficiency, durability, and scalability. Continued progress will depend on integrating advances in materials synthesis, *operando* characterization, computational modeling, and reactor engineering. When some of these challenges are addressed, oxy-sulfides may play an important role in future solar-fuel and electrolytic hydrogen technologies.

6. Conclusions

Oxy-sulfides constitute a distinctive class of materials that combine key advantages of oxides and sulfides. By integrating the structural and chemical stability typically associated with oxides with the narrower band gaps and enhanced electronic conductivity characteristic of sulfides, they have emerged as promising candidates for both electrocatalytic and photocatalytic water splitting. Examples ranging from NiFe-based oxy-sulfides for the hydrogen evolution reaction to layered titanate oxy-sulfides for visible-light-driven overall water splitting demonstrate that, like in traditional thermally driven catalysts, control of composition, microstructure, and heterostructure interfaces can significantly influence catalytic activity, carrier dynamics, and durability.

At the same time, this review highlights that important challenges remain. In photocatalysis, STH efficiencies in pure-water systems remain well below the levels generally considered necessary for economic viability, indicating that charge recombination, limited light absorption, and surface reaction kinetics continue to impose fundamental constraints. In both electro- and photocatalytic environments, photocorrosion, sulfur loss, surface reconstruction, and gradual compositional drift remain key degradation mechanisms, while reliance on noble-metal cocatalysts and the complexity of some synthesis routes present additional barriers to large-scale implementation.

Several directions appear particularly promising for overcoming these limitations. Advances *in situ* and *operando* characterization, combined with computational modeling and data-driven materials discovery, are poised to provide a clearer understanding of active phases and degradation pathways. A defining strength of oxy-sulfides is their exceptional tunability. Through mixed-anion chemistry, including layered M–O and M–S frameworks as well as hetero-anionic coordination environments, it is possible to tailor band structures, internal electric fields, and catalytic active sites in ways that are difficult to achieve in single-anion materials. This flexibility provides a powerful platform for optimizing the balance between activity and stability, which remains one of the central challenges in catalytic water splitting.

Ultimately, translating laboratory-scale demonstrations into practical hydrogen-production technologies will require progress in materials design, scalable synthesis, long-term stability under realistic operating conditions, and integrated reactor engineering. Continued advances in these areas may enable oxy-sulfide materials to play an important role in future solar-fuel and electrolytic hydrogen systems and to contribute meaningfully to the broader transition toward sustainable energy.

Author contributions

M. A. and O. T. designed, conceptualized and wrote the whole manuscript. M. Z., N. N., and H. I. revised the main manuscript

text. T. D., N. K and Y. T. wrote the sections and prepared Fig. 1–9 and Table 1. All authors reviewed the manuscript.

Conflicts of interest

Competing interests, The authors declare that they have no Conflicts of interests.

Data availability

No primary research results, software or code have been included and no new data were generated or analysed as part of this review.

Acknowledgements

This work was supported by the Ministry of Education and Science of the Republic of Kazakhstan under Grant No. AP23488359. Authors would like to acknowledge the support of the Ministry of Science and Higher Education of the Republic of Kazakhstan under Grant No. AP23488359.

References

1 P. R. Anusuyadevi, *et al.*, Fundamentals of Green Hydrogen through Photocatalysis - Current Insights into Scalability, *ACS Symp. Ser.*, 2024, **1467**, 137–164, DOI: 10.1021/bk-2024-1467.ch007.

2 H. Araújo, B. Šljukić, S. Gago and D. M. F. Santos, The current state of transition metal-based electrocatalysts (oxides, alloys, POMs, and MOFs) for oxygen reduction, oxygen evolution, and hydrogen evolution reactions, *Front. Energy Res.*, 2024, **12**, 1373522, DOI: 10.3389/fenrg.2024.1373522.

3 N. Kumar, R. Aepuru, S. Y. Lee and S. J. Park, Advances in Catalysts for Hydrogen Production: A Comprehensive Review of Materials and Mechanisms, *Nanomaterials*, 2025, **15**, 256, DOI: 10.3390/nano15040256.

4 D. S. Mallapragada, E. Gençer, P. Insinger, D. W. Keith and F. M. O'Sullivan, Can Industrial-Scale Solar Hydrogen Supplied from Commodity Technologies Be Cost Competitive by 2030?, *Cell Rep. Phys. Sci.*, 2020, **1**(9), 100174, DOI: 10.1016/j.xcrp.2020.100174.

5 T. Hisatomi, *et al.*, Photocatalytic water splitting for large-scale solar-to-chemical energy conversion and storage, *Front. Sci.*, 2024, **2**, 1411644, DOI: 10.3389/fsci.2024.1411644.

6 C. Bie, L. Wang and J. Yu, Challenges for photocatalytic overall water splitting, *Chem*, 2022, **8**(6), 1567–1574, DOI: 10.1016/j.chempr.2022.04.013.

7 A. Kazemi, F. Manteghi and Z. Tehrani, Metal Electrocatalysts for Hydrogen Production in Water Splitting, *ACS Omega*, 2024, **9**, 7310–7335, DOI: 10.1021/acsomega.3C07911.

8 Q. Zhu, *et al.*, Recent Progress of Metal Sulfide Photocatalysts for Solar Energy Conversion, *Adv. Mater.*, 2022, **34**(45), 2202929, DOI: 10.1002/adma.202202929.

9 L. Lin, *et al.*, Efficient and stable visible-light-driven Z-scheme overall water splitting using an oxysulfide H2 evolution photocatalyst, *Nat. Commun.*, 2024, **15**(1), 1–12, DOI: 10.1038/s41467-024-44706-4.

10 K. A. Wahab and H. Idriss, Hydrogen Production During Ethylene Glycol Photoreactions Over Ag-Pd/TiO2 at Different Partial Pressures of Oxygen, *Int. J. Hydrogen Energy*, 2024, **52**, 159–171, DOI: 10.3389/fchem.2019.00780.

11 J. L. Giocondia, P. A. Salvador and G. S. Rohrer, The Origin of Photochemical Anisotropy in SrTiO3, *Top. Catal.*, 2007, **44**(4), 529–533, DOI: 10.1007/s11244-006-0101-y.

12 M. Alrushaid, K. A. Wahab, M. A. Nadeem and H. Idriss, Extracting Turn Over Frequencies of Electron Transfer in Heterogeneous Catalysis: A Study of IrO2-TiO2 Anatase for Water Oxidation Using Ce4+ Cations, *Catalysts*, 2021, **11**(9), 1030, DOI: 10.3390/catal11091030.

13 M. Lanz, D. Schurch and G. Calzaferri, Photocatalytic Oxidation of Water to O2 on AgCl-coated Electrodes, *J. Photochem. Photobiol., A*, 1999, **120**, 105–117, DOI: 10.1016/S1010-6030(98)00434-1.

14 S. Nandy, T. Hisatomi, T. Takata, T. Setoyama and K. Domen, Recent Advances in Photocatalyst Sheet Development and Challenges for Cost-effective Solar Hydrogen Production, *J. Mater. Chem. A*, 2023, **11**, 20470–20479, DOI: 10.1039/d3ta04353c.

15 X. Zhang, S. Wang and S. Wang, Morphology, interface, and energy field engineering of ternary oxide photoanodes for efficient photoelectrochemical water splitting, *Mater. Chem. Front.*, 2026, **10**, 762–789, DOI: 10.1039/d5qm00838g.

16 S. Al Bacha, E. E. McCabe and H. Kabbour, Advances in oxychalcogenide materials for hydrogen evolution photocatalysis in aqueous media, *Chem. Commun.*, 2025, **61**, 11510–11528, DOI: 10.1039/d5cc01448d.

17 R. Miyoshi and T. Takata, Recent Progress in Mixed-Anion Materials for Solar Fuel Production, *Sol. RRL*, 2021, **5**(5), 2000521, DOI: 10.1002/solr.202000521.

18 H. Yoshida, *et al.*, An Oxysulfide Photocatalyst Evolving Hydrogen with an Apparent Quantum Efficiency of 30% under Visible Light, *Angew. Chem., Int. Ed.*, 2023, **62**(46), e202312938, DOI: 10.1002/anie.202312938.

19 N. Vonrüti and U. Aschauer, Band-gap engineering in AB(OxS1−x)3 perovskite oxysulfides: a route to strongly polar materials for photocatalytic water splitting, *J. Mater. Chem. A*, 2019, **7**(26), 15741–15748, DOI: 10.1039/c9ta03116b.

20 A. K. Watkins, A. K. Cheetham and R. Seshadri, Metallic Oxides and the Overlooked Role of Bandwidth, *Chem. Mater.*, 2026, **38**, 1551–1565, DOI: 10.1021/acs.chemmater.5c02578.

21 J. Portier, H. S. Hilal, I. Saadeddin, S. J. Hwang, M. A. Subramanian and G. Campet, Thermodynamic Correlations and Band Gap Calculations in Metal Oxides, *Prog. Solid State Chem.*, 2004, **32**, 207–217, DOI: 10.1016/j.progsolidstchem.2005.05.001.

22 Q. Wang, *et al.*, Oxysulfide Photocatalyst for Visible-Light-Driven Overall Water Splitting, *Nat. Mater.*, 2019, **18**, 827–832, DOI: 10.1038/s41563-019-0399-z.

23 Y. Al-Salik, K. Katsiev and H. Idriss, Electron Transfer from Excited Semiconductor to Metal Particles and Its Implication on Photocatalysis: The Case of Au/TiO2(110) Single Crystal, *J. Phys. Chem. C*, 2022, **126**, 15184–15190, DOI: 10.1021/acs.jpcc.2c04025.

24 Z. H. N. Al-Azri, A. Al-Oufi, A. Chan, G. I. N. Waterhouse and H. Idriss, Metal Particle Size Effects on the Photocatalytic Hydrogen Ion Reduction, *ACS Catal.*, 2019, **9**, 3946–3958, DOI: 10.1021/acscatal.8b05070.

25 G. R. Bamwenda, S. Tsubota, T. Nakamura and M. Haruta, Photoassisted hydrogen production from a water-ethanol solution: a comparison of activities of Au/TiO2 and Pt/TiO2, *J. Photochem. Photobiol., A*, 1995, **89**, 177–189, DOI: 10.1016/1010-6030(95)04039-I.

26 Materials Project, "*Materials Data on Y2Ti2S2O5*," 2020, DOI: 10.17188/1200585.

27 G. M. Tomboc, B. T. Gadisa, J. Joo, H. Kim and K. Lee, Hollow Structured Metal Sulfides for Photocatalytic Hydrogen Generation, *ChemNanoMat*, 2020, **6**(6), 850–869, DOI: 10.1002/cnma.202000125.

28 R. Li, *et al.*, Band-tail states meditated visible-light-driven overall water splitting in Y2Ti2O5S2 photocatalyst, *J. Mater. Chem. A*, 2022, **10**(45), 24247–24257, DOI: 10.1039/d2ta06315h.

29 X. Liang, *et al.*, Surface Modifications of Layered Perovskite Oxysulfide Photocatalyst Y2Ti2O5S2 to Enhance Visible-Light-Driven Water Splitting, *Advanced Science*, 2025, **12**(3), 2412326, DOI: 10.1002/advs.202412326.

30 Z. Song, *et al.*, Visible-Light-Driven Photocatalytic Z-Scheme Overall Water Splitting in La5Ti2AgS5O7-based Powder-Suspension System, *ChemSusChem*, 2019, **12**(9), 1906–1910, DOI: 10.1002/cssc.201802306.

31 A. C. Estrada, J. L. Lopes, T. Trindade, A. C. Estrada, J. L. Lopes, and T. Trindade, "Nanomaterials of Carbon and Metal Sulfides in Photocatalysis," *Photocatalysts - New Perspectives*, Jan. 2023, doi: DOI: 10.5772/intechopen.109658.

32 A. Miura, T. Oshima and K. Maeda, Synthesis, Structure and Photocatalytic Activity of Layered LaOInS2, *J. Mater. Chem. A*, 2017, **5**, 14270–14277, DOI: 10.1039/c7ta04440b.

33 H. Kabbour, L. Cario, Y. Moelo and A. Meerschaut, Synthesis, X-Ray and Optical Characterizations of Two New Oxysulfides: LaInS2O and La5In3S9O3, *J. Solid State Chem.*, 2004, **177**, 1053–1059, DOI: 10.1016/j.jssc.2003.10.012.

34 S. Chen, L. Ma, Z. Huang, G. Liang and C. Zhi, In situ/operando analysis of surface reconstruction of transition metal-based oxygen evolution electrocatalysts, *Cell Rep. Phys. Sci.*, 2022, **3**(1), 100729, DOI: 10.1016/j.xcrp.2021.100729.

35 L. Gastaldi, D. Carre and M. P. Pardo, Structure de L'oxysulfure d'Indium et de Lanthane In6La10O6S17, *Acta Crystallogr., Sect. B*, 1982, **38**, 2365–2367, DOI: 10.1107/s0567740882008802.

36 J. Wang, *et al.*, Topological Modulation of Heteroanionic Motifs in a Novel Oxysulfide Sr3In4O4S5 for Synchronized Charge Dynamics and Enhanced Solar Fuel Generation, *Adv. Funct. Mater.*, 2026, e27508, DOI: 10.1002/adfm.202527508.

37 D. Tetzlaff, *et al.*, [NiFe]-(Oxy)Sulfides Derived from NiFe2O4 for the Alkaline Hydrogen Evolution Reaction, *Energies*, 2022, **15**(2), 543, DOI: 10.3390/en15020543/S1.

38 C. Kim, *et al.*, Promoting electrocatalytic overall water splitting by sulfur incorporation into CoFe-(oxy)hydroxide, *Nanoscale Adv.*, 2021, **3**(22), 6386–6394, DOI: 10.1039/d1na00486g.

39 P. V. Sarma, *et al.*, Nanostructured Tungsten Oxysulfide as an Efficient Electrocatalyst for Hydrogen Evolution Reaction, *ACS Catal.*, 2020, **10**(12), 6753–6762, DOI: 10.1021/acscatal.9b04177.

40 S. Yaseen, M. B. Tahir and A. G. Wattoo, Photocorrosion inhibition of sulphide-based nanomaterials for energy production through photocatalytic water splitting, *Int. J. Energy Res.*, 2022, **46**(2), 634–666, DOI: 10.1002/er.7276.

41 N. A. Khan, *et al.*, Boosting electrocatalytic hydrogen generation from water splitting with heterostructured MoS2/NiFe2O4 composite in alkaline media, *Int. J. Hydrogen Energy*, 2024, **69**, 261–271, DOI: 10.1016/j.ijhydene.2024.05.042.

42 B. Q. Li, S. Y. Zhang, C. Tang, X. Cui and Q. Zhang, Anionic Regulated NiFe (Oxy)Sulfide Electrocatalysts for Water Oxidation, *Small*, 2017, **13**(25), 1700610, DOI: 10.1002/smll.201700610.

43 K. C. Majhi and M. Yadav, Transition Metal-Based Chalcogenides as Electrocatalysts for Overall Water Splitting, *ACS Eng. Au*, 2023, **3**(5), 278–284, DOI: 10.1021/acsengineeringau.3c00014.

44 F. D. Speck, A. Zagalskaya, V. Alexandrov and S. Cherevko, Periodicity in the Electrochemical Dissolution of Transition Metals, *Angew. Chem., Int. Ed.*, 2021, **60**(24), 13343–13349, DOI: 10.1002/anie.202100337.

45 V. Dias, H. Maciel, M. Fraga, A. O. Lobo, R. Pessoa and F. R. Marciano, Atomic Layer Deposited TiO2 and Al2O3 Thin Films as Coatings for Aluminum Food Packaging Application, *Materials*, 2019, **12**, 682, DOI: 10.3390/ma12040682.

46 S. S. Kahandal, *et al.*, A review on chalcogenides nanomaterials for electrocatalysis: Insights into structural and compositional development, *J. Ind. Eng. Chem.*, 2025, **156**, 78–122, DOI: 10.1016/j.jiec.2025.08.050.

47 X. Ding, *et al.*, Dynamic restructuring of nickel sulfides for electrocatalytic hydrogen evolution reaction, *Nat. Commun.*, 2024, **15**(1), 1–11, DOI: 10.1038/s41467-024-49015-4.

48 W. Bao, *et al.*, Unveiling the Role of Surface Self-Reconstruction of Metal Chalcogenides on Electrocatalytic Oxygen Evolution Reaction, *Adv. Funct. Mater.*, 2024, **34**(48), 2408364, DOI: 10.1002/adfm.202408364.

49 Y. Zhao, *et al.*, Self-Templating Strategies for Transition Metal Sulfide Nanoboxes as Robust Bifunctional Electrocatalysts, *Chem. Mater.*, 2020, **32**(4), 1371–1383, DOI: 10.1021/acs.chemmater.9B02933.

50 D. O. Opar, R. Nankya, C. J. Raj and H. Jung, In-situ functionalization of binder-free three-dimensional boron-doped mesoporous graphene electrocatalyst as a high-

performance electrode material for all-vanadium redox flow batteries, *Appl. Mater. Today*, 2021, **22**, 100950, DOI: 10.1016/j.apmt.2021.100950.

51 X. Ning and G. Lu, Photocorrosion inhibition of CdS-based catalysts for photocatalytic overall water splitting, *Nanoscale*, 2020, **12**(3), 1213–1223, DOI: 10.1039/c9nr09183a.

52 Z. Liu, *et al.*, Photocorrosion suppression of copper sulfide *via* hybridization with amino-functionalized metal–organic framework for natural sunlight-driven photocatalysis, *Fuel*, 2024, **376**, 132721, DOI: 10.1016/j.fuel.2024.132721.

53 M. Li, *et al.*, Engineering interfacial sulfur migration in transition-metal sulfide enables low overpotential for durable hydrogen evolution in seawater, *Nat. Commun.*, 2024, **15**(1), 1–10, DOI: 10.1038/s41467-024-50535-2.

54 Y. Zhang, B. Liu, L. Xu, Z. Ding, R. Yang and S. Wang, Failure Mechanism Analysis and Emerging Strategies for Enhancing the Photoelectrochemical Stability of Photoanodes, *ChemSusChem*, 2025, **18**, e202401420, DOI: 10.1002/cssc.202401420.

55 Y. Kang, *et al.*, Binder-Free Electrodes and Their Application for Li-Ion Batteries, *Nanoscale Res. Lett.*, 2020, **15**(1), 1–19, DOI: 10.1186/s11671-020-03325-w.

56 T. Jin, Q. Han, L. Jiao, T. Jin, Q. Han and L. Jiao, Binder-Free Electrodes for Advanced Sodium-Ion Batteries, *Adv. Mater.*, 2020, **32**(3), 1806304, DOI: 10.1002/adma.201806304.

57 R. Zazpe, *et al.*, Atomic Layer Deposition Al2O3 Coatings Significantly Improve Thermal, Chemical, and Mechanical Stability of Anodic TiO2 Nanotube Layers, *Langmuir*, 2017, **33**(13), 3208–3216, DOI: 10.1021/acs.langmuir.7b00187.

58 Y. Liu, Y. Guo, Y. Liu, Z. Wei, K. Wang and Z. Shi, A Mini Review on Transition Metal Chalcogenides for Electrocatalytic Water Splitting: Bridging Material Design and Practical Application, *Energy Fuels*, 2023, **37**(4), 2608–2630, DOI: 10.1021/acs.energyfuels.2c03833.

59 T. Liang, Y. Liu, Y. Cheng, F. Ma and Z. Dai, Scalable Synthesis of a MoS2/Black Phosphorus Heterostructure for pH-Universal Hydrogen Evolution Catalysis, *ChemCatChem*, 2020, **12**(10), 2840–2848, DOI: 10.1002/cctc.202000139;subpage:string:full.

60 Y. Song, *et al.*, Heterojunction Engineering of Multinary Metal Sulfide-Based Photocatalysts for Efficient Photocatalytic Hydrogen Evolution, *Adv. Mater.*, 2024, **36**(11), 2305835, DOI: 10.1002/adma.202305835.

61 Z. Shalabayev, *et al.*, Sustainable Scalable Mechanochemical Synthesis of CdS/Bi2S3 Nanocomposites for Efficient Hydrogen Evolution, *Nanomaterials*, 2024, **14**(22), 1785, DOI: 10.3390/nano14221785/S1.

62 Q. Wu, *et al.*, A molybdenum sulfo-oxide/cobalt oxysulfide Z-scheme heterojunction catalyst for efficient photocatalytic hydrogen production and pollutant reduction, *J. Mater. Chem. A*, 2022, **10**(10), 5328–5349, DOI: 10.1039/d1ta09053d.

63 J. Huang, *et al.*, High-efficiency and stable photocatalytic hydrogen evolution of rhenium sulfide co-catalyst on Zn0.3Cd0.7S, *Mater. Adv.*, 2020, **1**(3), 363–370, DOI: 10.1039/d0ma00187b.

64 Y. Sun, B. Wang, X. Liu, L. Gao and W. Shangguan, Synthesis of Ternary Cross-Linked MoS2/WS2/CdS Photocatalysts for Photocatalytic H2 Production, *Catalysts*, 2023, **13**, 1149, DOI: 10.3390/catal13081149.

65 Y. Liu, *et al.*, Photocatalytic Hydrogen Evolution Using Ternary-Metal-Sulfide/TiO2 Heterojunction Photocatalysts, *ChemCatChem*, 2022, **14**(5), e202101439, DOI: 10.1002/cctc.202101439.

